The University of Maine

DigitalCommons@UMaine

Electronic Theses and Dissertations   Fogler Library

Spring 5-20-2021

Manipulation of Particles and Fluid with Surface Acoustic Waves

Joel Scott Tewksbury
University of Maine, joel.tewksbury@maine.edu

Recommended Citation

MANIPULATION OF PARTICLES AND FLUID WITH SURFACE ACOUSTIC WAVES

By

Joel Scott Tewksbury

B.S., Duke University, 2018

A DISSERTATION/THESIS

Submitted in Partial Fulfillment of the

Requirements for the Degree of

Master of Science

(in Biomedical Engineering)

The Graduate School

The University of Maine

May 2021

Advisory Committee:

      Dr. Caitlin Howell, Assistant Professor of Chemical and Biomedical Engineering,

      Advisor

      Dr. Mauricio Pereira da Cunha, Professor of Electrical and Computer Engineering,

      Advisor

      Dr. Andre Khalil, Professor of Chemical and Biomedical Engineering,

MANIPULATION OF PARTICLES AND FLUID WITH SURFACE ACOUSTIC WAVES

By Joel Tewksbury

Thesis Advisors: Dr. Caitlin Howell and Dr. Mauricio Pereira da Cunha

An Abstract of the Thesis Presented
in Partial Fulfillment of the Requirements for the
Degree of Master of Science
(in Biomedical Engineering)
May 2021

Small biomolecules can be challenging and expensive to isolate and manipulate, but they may be the key for developing more efficient diagnostic tools for the detection of biomarkers, such as those associated with pancreatic cancer. Pancreatic cancer has a survival rate of less than 10% five years after diagnosis. For this reason, the research and establishment of cheap, effective screening tools are highly desired. One promising method of screening is separating and identifying biomarkers in a patient's blood that are indicative of pancreatic cancer. The purpose of this project is to develop a system using surface acoustic waves (SAWs), in conjugation with microfluidics and surface functionalization, to manipulate small molecules and droplets with the goal of enabling the system to isolate particles within the blood. The separation and manipulation are achieved by passing the targeted fluidic material, in this case blood, through a microfluidic channel on top of a SAW device. The SAWs are generated by using an array of interdigital transducers (IDTs) photolithographically printed on a piezoelectric crystal to convert the electrical signal into acoustic waves. The SAW propagates, guided at the top surface of the material, and interacts with the fluid, exerting a force on the fluid and on particles in solution. Using open microfluidics to manipulate fluid droplets as an alternative to a continuous flow stream in an enclosed microfluidic channel is also an option. Functionalizing the surface using a

fluorinated silane and coating with a fluorinated oil creates a liquid layer for easy droplet manipulation. The results of implementing this procedure shows dewetting of the oil layer, but despite this the liquid coating did provide a surface hydrophobic enough to allow for easy droplet sliding. This procedure combined with a heat source allows for concentration of particles at specific locations for easier particle detection. The development of the device discussed is expected to help yield a new and consistent approach to biologic particle manipulation methods that is both compact and more sensitive to facilitate the detection of diseases such as pancreatic cancer long before symptoms appear.

ACKNOWLEDGEMENTS

TABLE OF CONTENTS

LIST OF FIGURES

LIST OF TABLES

CHAPTER 1:

INTRODUCTION

Pancreatic cancer affects roughly 60,000 people in the US every year and has been increasing by about 1% each year since 2000[1]. The five year survival rate is an average of around 10%[1,2]. The main reason for this is that pancreatic cancer is asymptomatic until late stages of the disease. Once it reaches this point, treatment methods are not very effective. If caught early the five year survival rate jumps to around 39% but only a small percentage of individuals are diagnosed at this stage[2]. Treatment options include resection, radiation therapy, and chemotherapy. Only around 20% of patients are able to have a resection and those who have one only have a five year survival rate of 25%[3]. Pancreatic tumors also tend to be widespread and resistant to chemotherapy and radiation therapy[3]. Beyond improving current treatment methods the screening of at risk populations is key to increasing the survival rate. Current screening methods include biomarker blood tests and imaging. While these work they have low sensitivity with biomarker tests having a sensitivity in the 70-80% range and the imaging having a sensitivity below 70%[4]. Biomarker tests are the most promising and there are a few options to choose from. Current screening tests look for the CA19-9 antigen but more recently nucleic acids, exosomes, and circulating tumor cells (CTCs)[2–4]. Through the manipulation of the biomarkers targeted in the blood screening tests we hope to be able to increase the sensitivity of these tests and improve the outlook of this grim disease.

Precise manipulation of particles and fluid on the micro and nano scale is of significant interest in the field of biomedicine. Acoustics is one such technology that seems promising for this application[5–13]. Depending on the type of crystal and orientation used, different types of surface acoustic waves (SAW) guided at the surface can be excited. This includes shear

horizontal waves and Rayleigh waves (Figure 1)[14]. SAWs transverse to the direction of propagation and parallel to the surface are called shear or transverse waves, while SAWs that have particle displacement in the sagittal plane are known as Rayleigh waves. In contrast, Bulk Acoustic Waves (BAW) travel in the bulk of the material. The SAW energy is confined at the surface, thus allowing the partial transfer of that energy to materials on the surface. In that way SAW can interact with objects on the surface allowing for various applications discussed in this thesis.
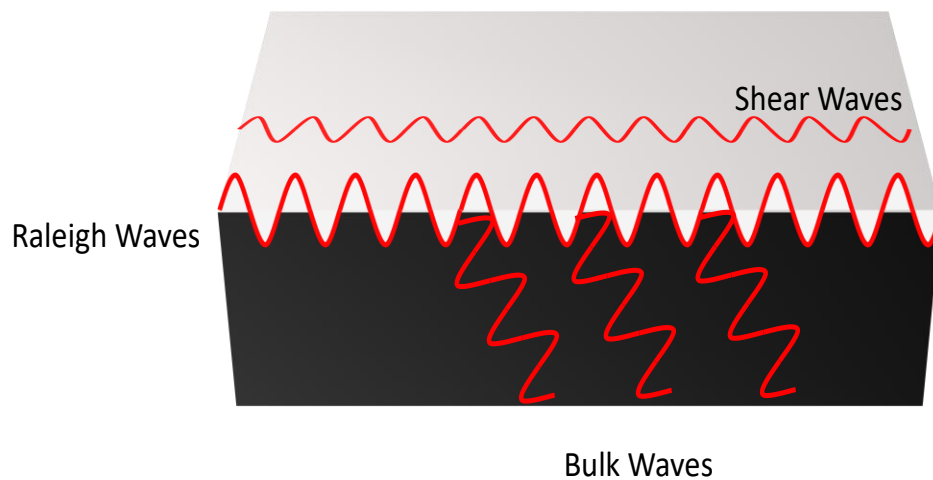
Figure 1. Examples of types of acoustic waves. They are Shear Plane Waves, and Raleigh Waves. Bulk Acoustic Waves are also shown propagating into the material.

Currently one of the most common uses for SAW is in communication systems, such as mobile phones. Since the 1960s, SAW devices have been researched and implemented in order to introduce signal delays, create resonators, and as bandpass filters[15–19]. More recently, SAWs have been implemented in chemical and biological systems[7,9,11,12,14–16,20–23]. They can be used for sensing of gases[22,24], organisms[11,25], small biomolecules such as nucleic acids[12,26], cell lysis[13], creating aerosols and nanoparticles[27,28], and manipulating liquid droplets or particles within a solution[29–35].

1.1 SAW Properties and Mechanisms

The concepts behind how SAW works are fairly simple but lead to a system with many complexities. SAW devices usually consist of a piezoelectric crystal or thin film, such as lithium niobate, lithium tantalate, quartz, aluminum nitride, and zinc oxide, with a thin film of conducting metal on top forming a transducer (Figure 2A). When a radio frequency (RF) signal is applied to the electrode it creates an electric field. This electric field causes the surface of the piezoelectric material to expand and contract, as shown in Figure 2B[14]. The reverse also occurs, as a deformation in the substrate material will generate an electric field which can be converted into an electric signal by the interdigital transducer (IDT)[36–38]. The substrate particle displacement caused by the electric field, in the case of these Rayleigh wave, follows an elliptical trajectory[39]. This results in a large normal force component that allows for the transfer of energy to materials on the surface. That's why Rayleigh waves are often used to manipulate particles and fluids (Figure 2B). Shear waves, on the other hand, are used when attenuation due to the liquid needs to be minimized, such as in sensor applications[9,11,15,22,23].The acoustic wave

Figure 2. Creation and propagation of SAW through a piezoelectric substrate. A) Shows the overall structure and basic setup of the IDTs on the surface. V_{RF} is the input RF signal, R_g is the system impedance (50Ω), p is the period, and W is the aperture. B) Shows the deformation of the surface in response to the electric field as well as energy transferring to liquid or particles on the surface.

velocity in solids is around five orders of magnitude slower than electromagnetic waves, which allows these devices to introduce a signal time delay on the order of several microseconds over lengths of only millimeters[14,15,19,22]. The wave velocity and thus the delay can vary based on orientation of the SAW in the materials, as piezoelectric materials are often anisotropic. It is also important to note that a change in the wave velocity implies a change in the wavelength at a given frequency. That's why when designing a device to function at a particular target frequency it is important to keep the crystal orientation in mind.

An IDT is designed specifically for its application. For biological applications, IDTs are typically made with gold or platinum, due to good conductivity, reduced oxidation, and good biocompatibility[40,41].The periodicity (p), and the aperture (W) of the IDT electrodes dictate the frequency response of the SAW device. For a regular single pair IDT each electrode polarity repeats every wavelength, thus leading to an electrode periodicity of $2p$ per wavelength, where p is the period or distance between opposite poles (Figure 3A)[14,18]. The relative position of the IDTs is used to obtain the desired acoustic wave. Two IDTs facing each other can be used, not only as a delay line, but also to generate SAWs that add constructively and destructively, creating nodes and maxima of particle displacement, commonly referred to as a standing surface acoustic wave (SSAW)[42–44].

Reflections from the substrate borders or the other IDTs cause signal regeneration in the IDT, generating spurious signals in the response[15,37,38,45]. One way to mitigate the effect of these wave reflections is to use a split finger design (Figure 3B). In this design each IDT finger is split half while keeping the wavelength ($\lambda = 2p$) the same. This design causes the reflections within the IDTs to add out of phase, reducing the spurious effects. Acoustic absorbers can also be added to the borders to absorb the wave before it can reach the point of reflection[15,37]. There are many

other designs of IDTs that assist with many other types of reflections and spurious effects[37,38,45], the details of which can be found elsewhere[37].
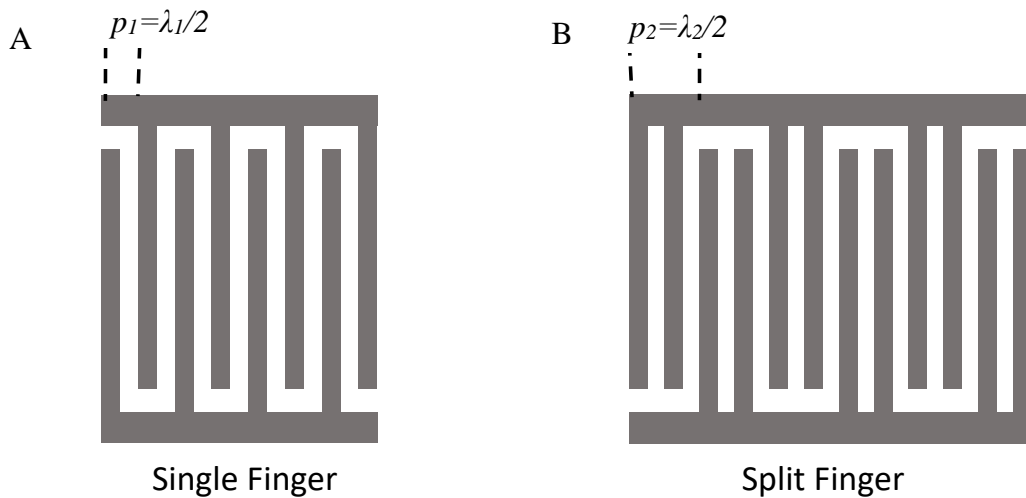
Figure 3. Interdigital transducer structure. A) A simple single finger IDT and a slightly more complex B) split finger design. The split finger design helps to reduce in phase reflections, thus producing a cleaner signal. The variable p is defined as the period of the IDT or the distance between fingers of opposite polarity.

1.2 Energy Transfer and Manipulation

When the SAW propagating at the surface of the substrate hits an object, part of the SAW wave energy refracts into that object, in what is known as a leakage wave. When the object is a fluid the leakage wave manifests as longitudinal pressure waves[6,11,33,39,46–49], since the molecules in a liquid slip past each other and do not allow shear waves to propagate. This leakage wave, depicted in Figure 4, propagates into the liquid at an angle from the normal given by[6,49]

$$\theta_R = \arcsin\left(\frac{c_1}{c_2}\right) \tag{1}$$
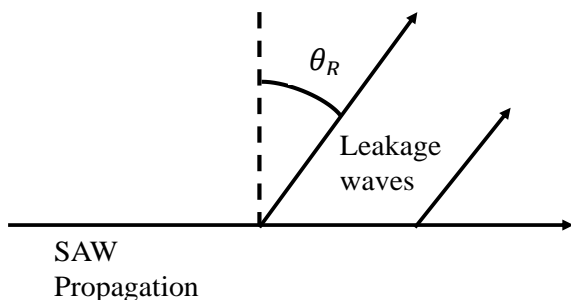
Figure 4. SAW leakage waves into a fluid on the surface. Waves propagate in at an angle θ_R

where θ_R is the Rayleigh angle, c_2 is the wave velocity in the substrate, and c_1 is the wave velocity in the liquid[6,49]. The leakage waves allow for the different types of applications mentioned earlier such as separation, patterning, mixing, and lysing. The fluid mechanics of the streaming caused by SAW are described by Vanneste et al. 2011[48].

Materials such as thin films, liquids, and biomolecules with different acoustic properties can be used to slow the SAW down, speed it up, generate BAWs into the crystal, reflect the wave, scatter, and/or severely attenuate the wave[50,51]. These effects can be useful in controlling and containing the acoustic wave on the device. For example, reflectors can be used to keep the energy from the SAW in the desired area and attenuators can be used to diminish the effects of unwanted reflections and noise. However, these effects can be of benefit or a hindrance depending on the application and location. In microfluidic devices the reflection and attenuation from the channel walls reduce the signal that is transferred to the liquid inside a chamber. For this reason, the selection of material for chamber walls is key, as further discussed in Section 2.4.2.

The flow streams within a liquid created by the leakage waves will exert a force on the particles that are in solution. The force acting on the particles depends on the particle size among other parameters as expressed by[49]

$$F_{TSAW} \approx 2\pi\rho_f A^2 \left(\frac{kR}{2}\right)^6 \left[\frac{1+\frac{2}{9}(1-(\frac{\rho_f}{\rho_p})^2)}{2+(\frac{\rho_f}{\rho_p})^2}\right], \tag{2}$$

where ρ_f is the fluid density, ρ_p the particle density, A the wave amplitude, R the radius of the particle, and k the wavenumber ($2\pi/\lambda$). While a traveling surface acoustic wave (TSAW) will launch a leak wave that imposes a constant acoustic force into the liquid, a SSAW will create acoustic forces that vary depending on location (Figure 6B). This is due to constructive and

destructive interference that take place due to the counter-propagating waves (Figure 6C). No

force is transmitted into the liquid in spots where the waves interact completely destructively

(180° out of phase) leading to the absence of substrate particle displacement. These regions,

called pressure nodes, tend to trap the particles. The force exerted on a particle due to a standing

wave is given by[52]

$$F_{SSAW} = -\left(\frac{\pi p_0^2 V_p \beta_0}{2\lambda}\right)\phi(\beta,\rho)\sin(2kx), \tag{3}$$

where

$$\phi(\beta,\rho) = \frac{5\rho_p - 2\rho_0}{2\rho_p + \rho_0} - \frac{\beta_p}{\beta_0} \tag{4}$$

and V_p is the particle volume, β_0 the fluid compressibility, β_p the particle compressibility, p_0 the

pressure wave amplitude, ρ_0 the fluid density, ρ_p the particle density, λ the wavelength of the

SSAW, k the wave vector, and x the distance from a pressure node. The leakage waves from the

SSAW compress and decompress the particles. The compressibility and density determine the

compressibility factor (Equation 4) which determines the direction of the net force due to these compression cycles[53–55]. Particles will either be drawn to the nodes or antinodes depending on the factor's sign. Most compressible solid particles, including cells and exosomes, will have positive compressibility factors drawing them to the nodes and not the anti-nodes[54]. Figure 5 shows a generic acoustic radiation force curve from Equation 3.

Figure 5. Acoustic radiation force. The acoustic force curve from a SSAW for one SAW wavelength. Nodes and anti-nodes are marked along with the direction of the net force of a particle in solution assuming a positive compressibility factor.

Acoustic forces are not the only forces acting on a moving particle in a fluid. Viscous drag can also have a significant effect, and can be calculated using the equation[20]

$$F_v = -6\pi\eta R v \tag{5}$$

where η is the viscosity, R the particle radius, and v the particle velocity. It is important to note that the acoustic radiation force from both TSAW and SSAW is proportional to a power of the particle radius while the drag force is proportional to the radius. This means that the larger the particle, the less significant the drag force becomes when compared to the acoustic force (Figure 6A). In other words, larger particles will be subjected to a much larger a net force, and accelerate faster in the direction of propagation of the wave than smaller particles. This is the fundamental concept that allows particles to be sorted by size using SAWs and shown in Figure 6A.
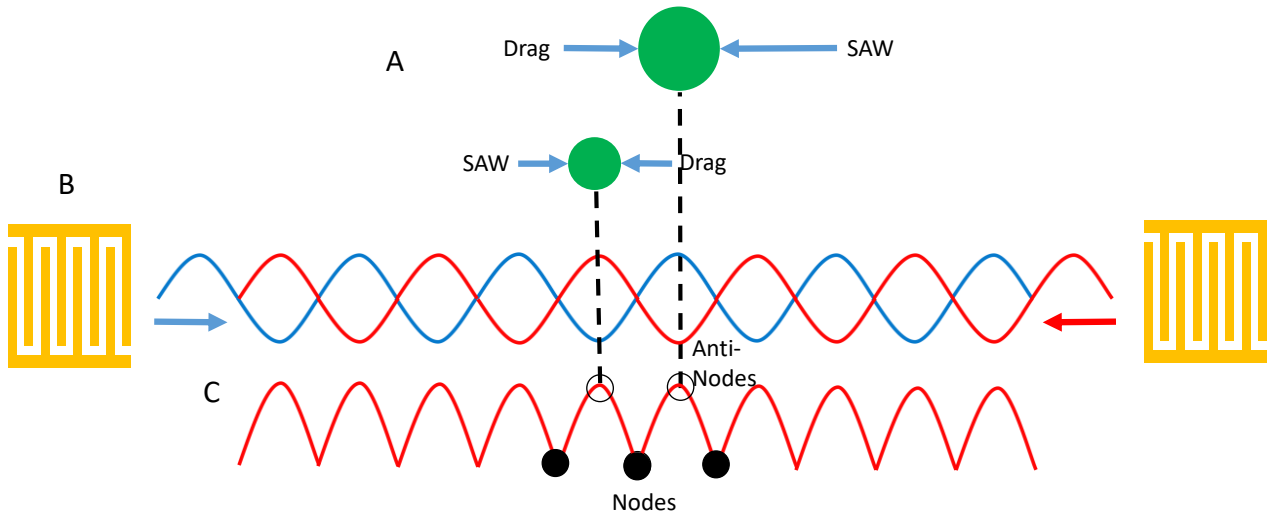
Figure 6. Standing surface acoustic wave particle manipulation. A) Forces acting on the particles in the plane of SAW propagation. The ratio of acoustic force to drag force is larger for large particles than smaller particles B) A SSAW propagating from two IDTs facing each other. C) The interference pattern of the SSAW that shows pressure nodes and anti-nodes over one wavelength.

1.3 Biological Applications

There are many amazing applications of SAWs in the field of biomedicine (Figure 7). For example, particle sensing involves trapping particles on the surface of a SAW device and observing the changes in the frequency, phase, delay, and/or attenuation response due to the film on the surface[11,12,25]. The surface may be treated with nucleic acid target-capture films that retain the targeted particles[12,23,56–58], giving the specificity to the SAW sensor platform. Antibodies which selectively bind specific proteins have also been immobilized on the surface of the SAW devices
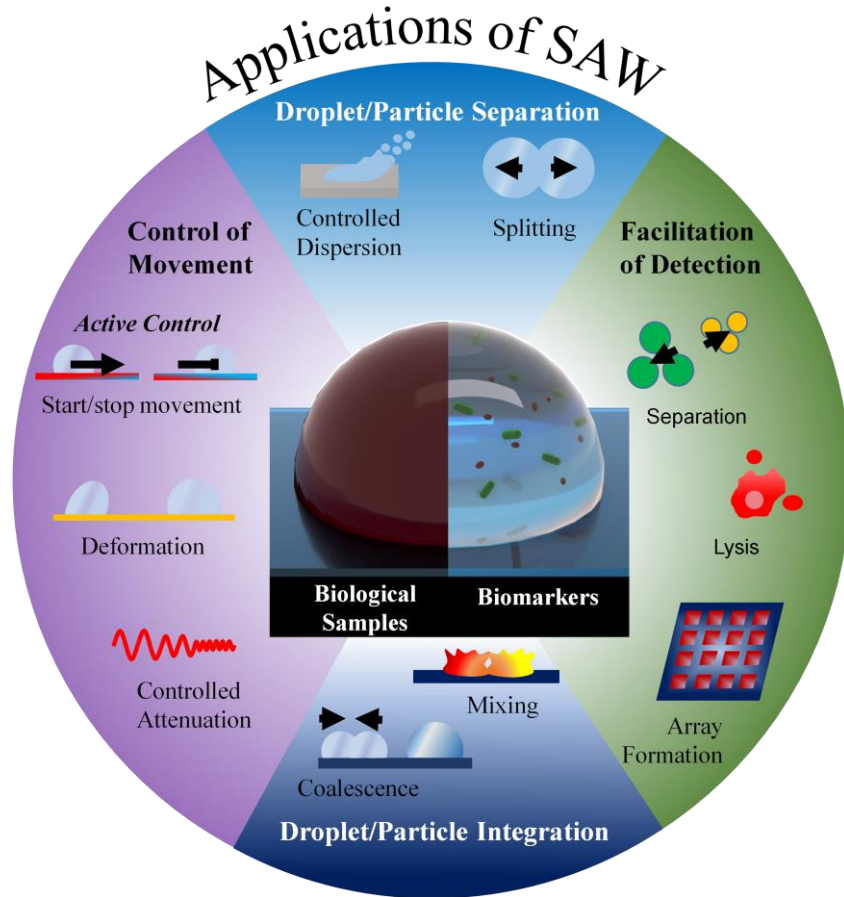
Figure 7. Biomedical applications of SAW devices. Primary applications of SAW in the field of biomedicine, divided into four main categories: Droplet/Particle Separation, Facilitation of Detection, Droplet/Particle Integration, and Control of Movement. Adapted from Regan and Howell 2019[88].

to serve in the detection of disease[25,59,60]. Loading the surface with attracted or immobilized particles results in an increase in mass as well as changes to the surface mechanical or electrical properties, including stiffness, conductivity, and/or viscosity[12,22,23,25]. These changes in the acoustic and/or electrical properties of the surface layer change the SAW phase velocity, which

is detected by either monitoring the frequency, phase, or amplitude response of the SAW delay line or resonator[11,22–24].

In addition to sensing biological molecules or particles on surfaces, SAWs can also be used to manipulate particles. Figure 8 shows the basic concept for a separation setup. Freely-suspended particles in solution can be manipulated by the acoustic force that is transmitted by the SAW into the fluid. This can be used for the separation and isolation of particles within a fluid as the acoustic force exerted differs depending on particle size as previously discussed in Section 1.2. This can be done with SSAW or TSAW. The scheme in Figure 8 is for a tilted SSAW. When tilted at the optimal angle of 15° the pressure nodes create diagonal paths towards one of the channel walls[61]. As the flow continues the particles get trapped in these paths and migrate towards the wall. Just like in the other separation schemes the larger particles are trapped in the nodes first and move the edge the fastest.
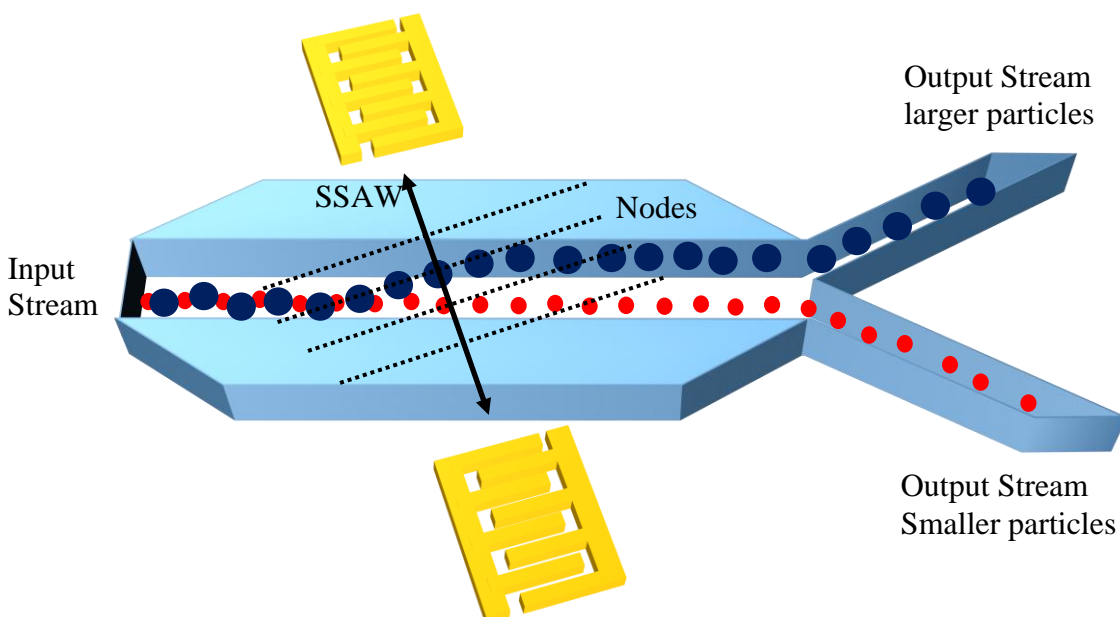
Figure 8. Simple particle separation scheme using SSAW. The particles enter the microfluidic channel mixed. An SSAW at an angle moves larger particles up towards the side of the channel along pressure node paths. After the SSAW has fully separated the particles, they exit in different channels.

Such particle manipulation via SAW is currently being used for label-free separation of particles of interest such as cells, pathogens, and various biomarkers like exosomes from blood[6,8,29,62]. Isolation of constituents from the blood can be useful for diagnosis of diseases, including difficult-to-detect cancers such as pancreatic cancer. Extracellular microvesicles, such as exosomes, contain molecules from their precursor cells and can be used as identifiers of the cells presence. However, due to their small size they are difficult to separate from solution, especially in small concentrations[63]. A SAW can be used to separate biological samples since it does not risk degrading the constituents and is able to work on sample volumes in the microliter range. Larger particles move to the pressure nodes of the SSAW while the small microvesicles stay in the center flow stream. In this way, SSAW can be used to separate the larger particles from solution leaving only the smaller microvesicles. Arrays of transducers can also be used to pattern the particles, trapping them in specified locations using the pressure nodes from SSAW[44,64]. A high enough acoustic force can even be used to lyse cells in solution, which can be useful for accessing cellular contents for further analysis[6,13,62].

As with particles in a fluid, small droplets of liquid can be manipulated with SAWs. Figure 9 shows some of the possible effects of SAW on droplets. If the acoustic force is greater than the surface adhesion forces, the droplet will move in the direction of the SAW. Often times surface functionalization along with liquid layers are required to make this possible and is discussed more in Chapter 4[65]. In this way the droplets can be translated and coalesced with the flow streams generated by the SAWs within the droplets, which also help to mix the droplet contents[10,40,47].
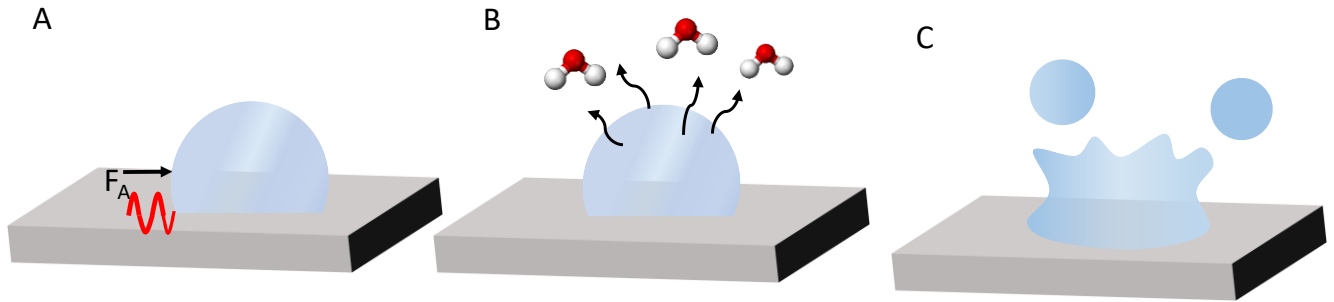
Figure 9. Different effects of SAW on liquid droplets. A) SAW can exert enough force to move a droplet along a designated path. B) The energy put into the droplet can cause it to evaporate. C) With enough energy the droplet will be split apart and/or jettison off the surface.

By mixing, moving and combining droplets, micro-sized chemical reactions contained within droplets can be performed[6,29,48,66]. Even if the acoustic force is not greater than the adhesion force, SAW energy is transferred into the droplet. High enough energy will lead to rapid evaporation or even droplet bursting[67–70], which can be useful for controlled aerosol release in applications such as in inkjet printing, drug delivery, and isolation of solids from liquid in droplets[68,71,72]. SAW-based droplet control strategies have also been used to produce nanoparticles[27,72]. Droplets can also be split by using two SAWs traveling in opposite directions[33]. Splitting is of particular interest as a way to concentrate samples: enriching cells and particles that are in low concentrations[30]. By isolating particles in a section of the droplet and then splitting that section off from the main volume the resulting droplet is enriched with a higher concentration of the particle of interest[30].

1.4 Goals

The goal of this project was to lay the groundwork for the advancement of surface acoustic wave devices both in terms of their effectiveness and in terms of their accessibility to the field of biomedicine. In order to do this two different functionalities of SAW were explored: the separation and manipulation of particles within a solution and microfluidic channel and the

manipulation of droplets in an open, channel free, system utilizing stable surface functionalization. We also designed a system that allows for easy plug-and-play functionality, increasing the ease of use for those unfamiliar with the technology. While not explored in this work, the hope is to incorporate this setup into pancreatic cancer diagnostics to improve their sensitivity to small circulating biomarkers.

Chapter 2:

SAW Device Design and Analyses

2.1 Introduction

The design of the SAW device and associated electronics is essential to successfully implementing the SAW in the desired application. There are several circuit design considerations that are necessary to properly transduce an electrical signal into the mechanical SAW waves. These considerations can be broken into four categories that are necessary in order to properly transmit an electrical signal to the IDT: power source, signal processing components, circuit board, and IDT (Figure 10). This chapter covers the design and analysis of the complete SAW system used in this project. First, the power entering the system from the signal generator needed to be determined. It must provide enough power to the system in order to run the SAW, but not too much or it risks damaging itself via power reflected back (Figure 10A). Secondly, the power coming from the synthesizer must be amplified and managed so that no component is damaged by spikes in current (Figure 10B). Third, there must be a circuit board that provides a stable electrical connection to the IDTs and allow for impedance matching to ensure maximum power is transferred into the IDTs (Figure 10C). The impedance matching circuit implemented contained reactive components (inductors and capacitors). Electrical connection between the IDT and the external circuit is typically done by bonding the wires directly to the IDT. In this work pogo pins have been used to allow for easy plug and play functionality, while also keeping a good electrical connection. Finally the IDT (Figure 10D) needed to be designed for the application. The frequency, cut and orientation of the piezoelectric substrate, material, type of IDT (single or split finger), aperture, number of fingers, and acoustic absorbers to minimize edge

reflections matter in the design of an IDT. This chapter further breaks down each of the four parts of the system and discusses how their parameters were decided and implemented.
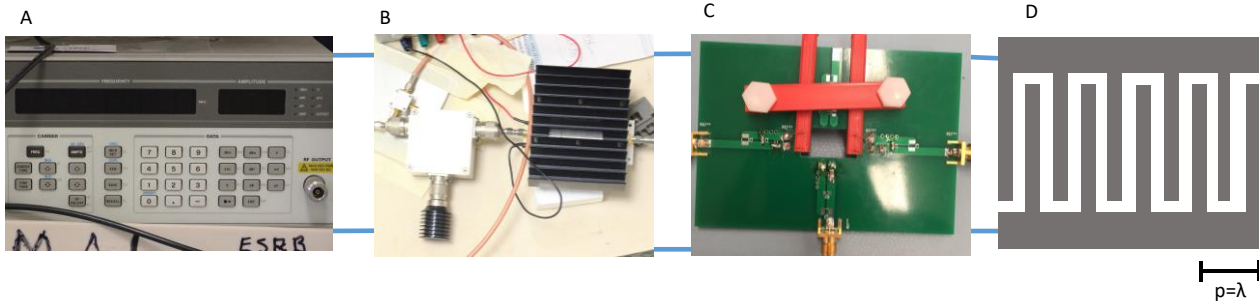
Figure 10. Components of a functioning SAW device system. A) The signal generator B) signal processing components, C) the circuit board and impedance matching circuit, along with pogo pins, and D) the IDT.

2.2 Materials and methods

2.2.1 New IDT Mask Design

The photomask was designed using AutoCAD software. The masks were designed as 5 in x 5 in chrome side up negative prints. The original 100 MHz SAW device (Figure 11A), designed by Tim Lyford[13,73], was a set of four split finger (Figure 3B) IDTs pairs with finger width of 4.7 μm. The new IDT design (Figure 11B) consisted of a split finger IDT with a finger width of 8.3 μm shown in Figure 11C. This spacing was chosen in order to achieve an operating frequency of around 60 MHz. There were two types of devices designed on this mask using this particular IDT structure. The devices were fabricated on lithium niobate Y-128° rotated wafers, Euler angles (0°,38°,Ψ). Two orientations Ψ=0° and Ψ=90° used. The first new device was a delay line in the Ψ=90° orientation and the second was a pair of orthogonal IDTs: one in the Ψ=0° orientation and one in the Ψ=90°. The aperture (W) of each IDT was 2.8 mm. The number of finger pairs of the IDTs in the Ψ=90° plane was 66, while the Ψ=0° plane IDTs had 32 finger pairs.

15
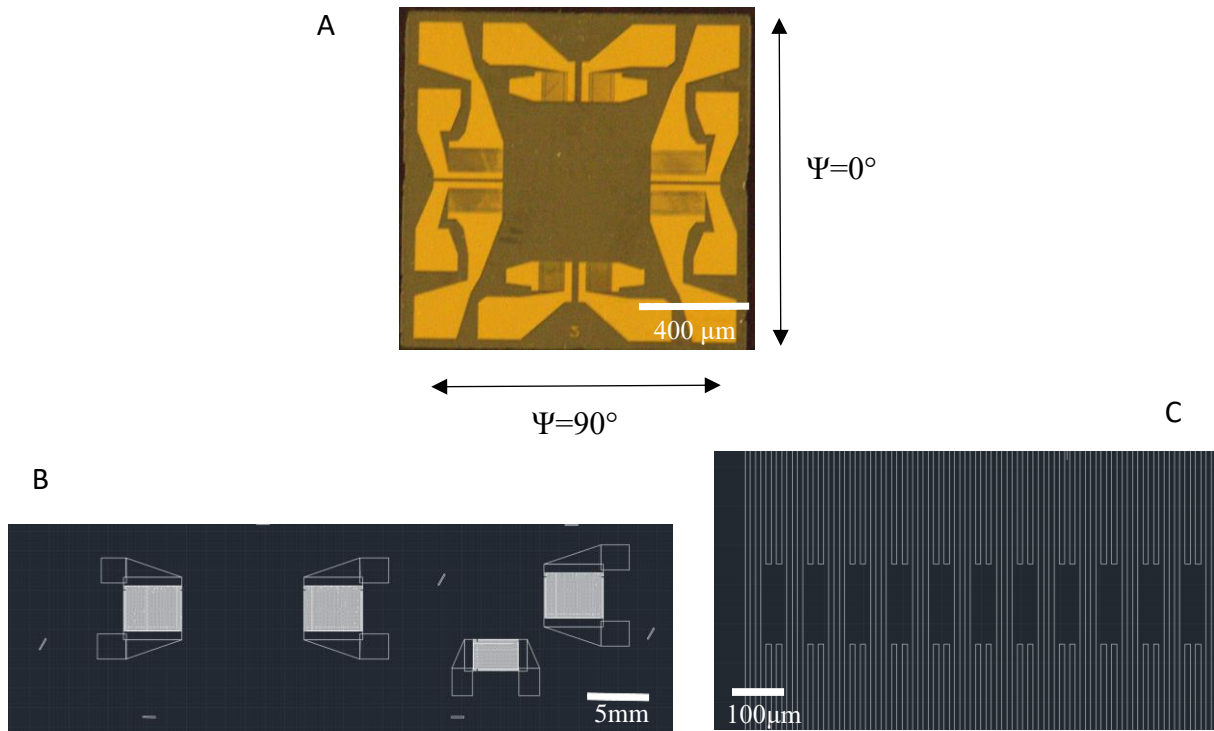
Figure 11. SAW devices. A) 100 MHz device with four sets of IDTs forming delay lines with 4.7 μm finger width[13,72]. B) 60 MHz devices. Delay line is on the left and the perpendicular pair is on the right. For both devices the Ψ=90° orientation is left to right while to Ψ=0° orientation is up and down. C) Close up of the split finger pair pattern with 8.3 μm finger width.

2.2.2 Device Manufacturing

SAW devices were manufactured using photolithography with negative photoresist in the Frontier Institute for Research in Sensor Technologies (FIRST) clean room by Michael Call. A dark field print photomask of the intended design was used to transfer the design to an optically polished four inch diameter lithium niobate (LiNbO₃) wafer. The IDT electrode structures consisted of a chromium adhesion layer followed by layer of gold. These structures were fabricated by a wet etch process.

2.2.3 Signal Generator

The signal generator or synthesizer with the regulatory electronics are shown in Figure 12[13,73]. The synthesizer was operated between -6 dBm and +2 dBm: a safe power range

that prevents too much power from flowing back to the amplifier in case the IDTs disconnect and all power is returned back. At +2dBm this applies 30 dBm to the output of the circulator. However, the synthesizer was typically operated at a power of -3 dBm. At this power the system provides approximately 24.7 dBm to a single SAW device. The signal from the signal generator first goes through a DC block, with an insertion loss of 0.5 dB, to filter out DC signals that could damage the synthesizer. The signal then goes through an amplifier with a gain of 29 dB. In order to prevent reflected signal from returning during a IDT disconnection and damaging the amplifier, a circulator directs forward power to the SAW device and returning power to a load with a max nominal input power characteristic of 10 W. The loss from the circulator was 0.8 dB. The circulator used depends on the operating frequency. For the 100 MHz devices the Wenteq F2816-0098-2D model was used and for the 60 MHZ devices the F2810-0055-15 model was used. When needed, a splitter divides the power between the two IDTs with an insertion loss of about 3.7 dBm to each port.
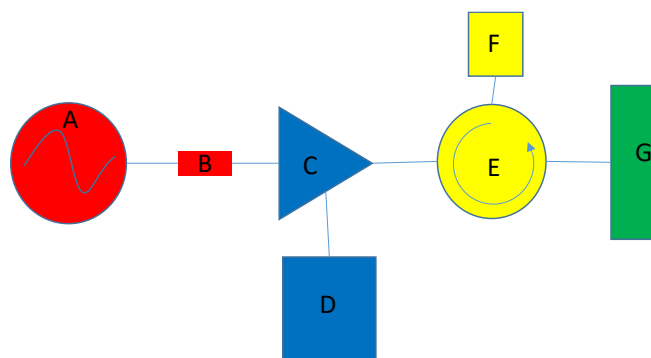
Figure 12. Electronics schematic. Schematic of the power supply and power control electronics adapted from Lyford et. al 2012. A) Agilent N9310A Signal Generator, B) DC block, C) RF Lambda 2HL-1-SW-S Amplifier, D) BK Precision 1761 DC Power Supply, E) Wenteq Circulator (F2816-0098-2D or F2810-0055-15), F) RFAC Solutions T580-10 Termination Load, and G) Circuit board[13,73]

2.2.4 Circuit Board Design

An FR4 circuit board was used to connect the SAW device to the signal
generation system via coaxial lines. Two clips were 3D printed with a Ultimaker 2+ using
polylactic acid (PLA) with a resolution of 0.06 mm. These were used to facilitate the electrical
connection by implementing pogo pins. The full board with pins is shown in Figure 13. The pins
were soldered to 0.27 mm diameter and approximately one cm long copper wires connected to
the circuit board. They were then inserted into the clips using glue or epoxy. SAW devices were
inserted into the board by lightly lifting up on the PLA clip and sliding the device underneath
with Teflon coated tweezers, making sure that the pogo pins contact the correct points without
touching the surface of the SAW device. The bracer was then screwed into the board evenly so
that neither side had too much pressure on it. When fully screwed in the bracer and clips setup
provided a stable electrical connection between the POGO pins and the IDTs. The board was
connected to the signal processing compoents by a SMA connector and coaxial line.
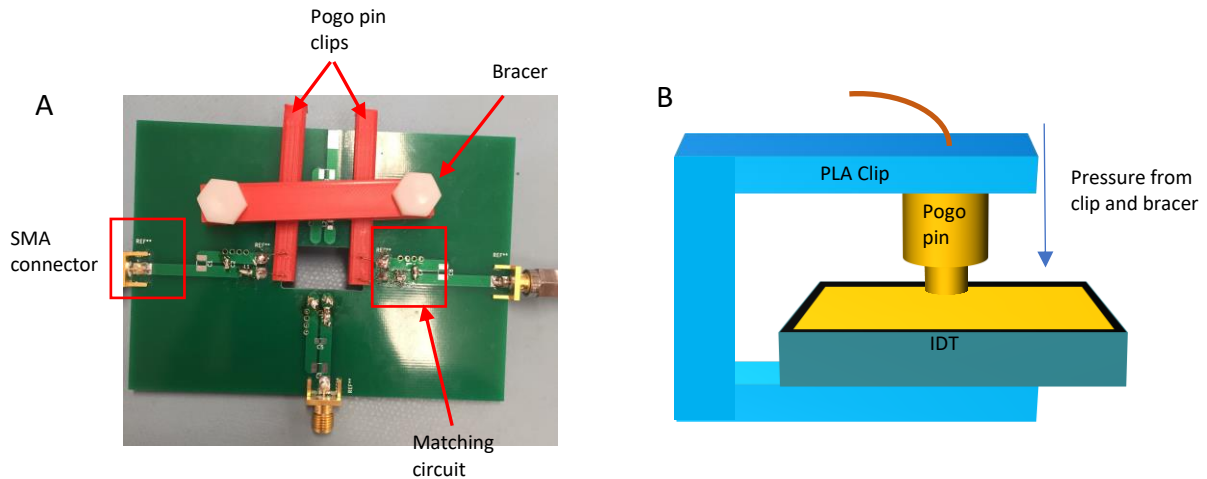
Figure 13. Circuit board and pogo pins. A) The circuit board with PDMS pins as viewed
from the top. Seen are the clips and bracer applying pressure, the matching circuit, and the
SMA connectors. B) A diagram of the concept behind the pogo pin setup. Pressure from the
clips and bracer provides the necessary physical contact between the POGO pin and IDT. It is
easy to insert and remove.

2.2.5 SAW Device Analysis

The devices were measured using an Agilent Technologies E5061B ENA series Network

Analyzer. The device was calibrated at the end of the coaxial cable. Phase correction was

performed using the POGO pins as a point of reference by shorting the two pogo pin connectors

with a piece of copper mesh and adding an electrical delay (1.2 ns) to bring the impedance to the

short point of the Smith chart. The short point for the measured S_{11} value being the leftmost point

of the Smith chart (Appendix)[74]. The S parameters were measured as a function of frequency

response for each device[75]. The frequency response for a SAW device should resemble a sinc

function with the center being the close to the designed operating frequency. Photoresist was

placed at the edges for all measurements, and in between IDTs for reflection measurements, to

act as acoustic absorbers and reduce unwanted reflections.

Impedance matching was conducted for all devices based on the frequency response data

measured. These values were plotted on a Smith chart using the circuit Design with Smith Cart

software[76] and then brought to the center of the chart using a reactive L matching network

(capacitors and inductors) in series and parallel. Detail on the implementation of this circuit are

discussed in Section 2.3. A detailed description of how to use a Smith Chart can be found in

Pozer 2011[75].

2.2.6 Attenuation and Force Calculations

The acoustic force acting on a particle in solution was calculated using Equations 3 and 4.

An attenuation coefficient at each frequency was calculated with Equation (5)[77] below and

solving for α in Equation (6),

$$A_x = A_0 e^{-\alpha x} \tag{5}$$

$$\alpha = -\ln(A_x/A_0)/x \tag{6}$$

where α is the attenuation coefficient, A_x is the current amplitude, A is the initial amplitude, and x is the thickness of PDMS that the wave travels through. The ratio of A_x/A_0 was extrapolated from a graph from Winkler et. al 2016 shown in Figure 14[78]. Plugging the resulting α back into Equation 5 with an x of 1 mm, the percentage of the pressure wave attenuated by one of our PDMS walls was determined. This value was then multiplied by the pressure wave amplitude in Equations 3 and 4 in order to factor in the attenuation into those equations.

Figure 14. Plot of power attenuation vs. frequency for PDMS with 0.1mm wall. Reproduced from Winkler et. al 2016[78].

The maximum time it takes to separate particles was determined by first assuming that the particles were always at local maximum velocity. Next the maximum velocity vs. distance from the pressure node curve was determined by setting the acoustic force (Equation 3) equal the drag force (Equation 5) at all distances (x). Then the time it takes to move from the antinode to the node was calculated by taking the integral of the inverse of the velocity with respect to distance (Equation 7),

$$t = \int \frac{1}{v(x)} dx \qquad (7)$$

where t is time and $v(x)$ is the velocity as a function of location.

2.3 Results

2.3.1 Circuit board and power transmission.

The reflection coefficients of five IDTs from the redesigned mask measured at 54.9 MHz are plotted in Smith charts in Figure 15. Each of the IDTs were measured at one of the two

coaxial input ports and then flipped around and measured at the other. Each Smith chart in Figure 15 shows the data from the same five IDTs but from one port each. The values are consistent regardless of this input port showing that the circuit board and POGO pins provide consistent electrical contact.

A

B
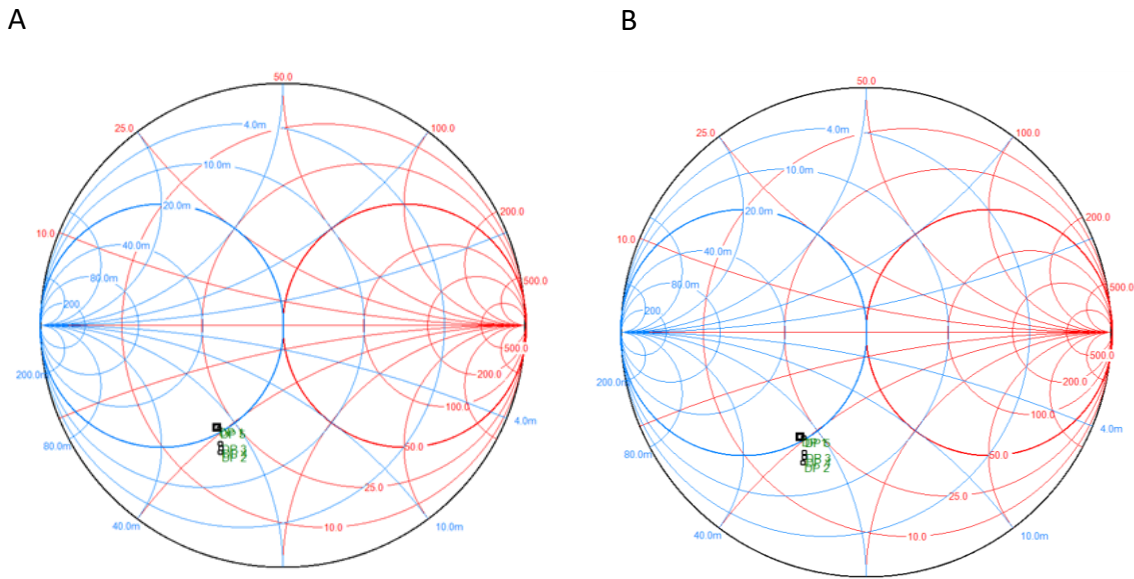
Figure 15. Reflection coefficient measurements. Plotted on a Smith chart for the same five IDTs from one port (A) and the other port (B). DPs1-6 as designators of individual IDTs on SAW devices like in Figure 10B. Point D1 in A is the same D1 as B simply measured on the other input port.

Figure 16 shows the Smith chart and corresponding matching circuits between the delay line IDTs and 50 Ω for both 100 MHz and 60 MHz devices at their operating frequency (Section 2.3.2) 96.8 and 54.9 respectively. Table 1 summarizes the results from the matching. With the values of reactive components available in the lab approximate values were selected for each device. For the 100 MHz it was a 150 nH inductor in series with the load, followed by s 27 pF capacitor in parallel, and for the 60 MHz devices it was 150 nH in series with the load followed by 68 pF in parallel.
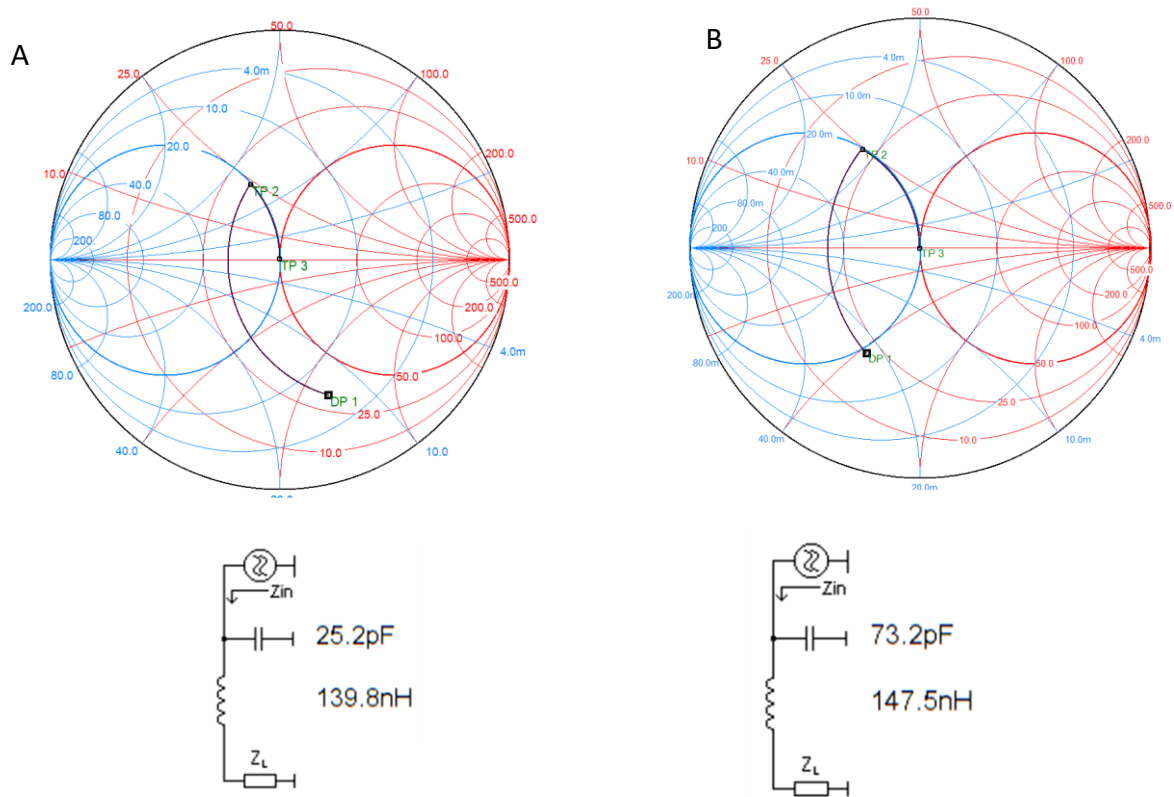
Figure 16. Impedance matching. The Smith charts and there corresponding matching circuits

for the (A) 100 MHz devices and the (B) 60 MHz devices.

Table 1: Reflection Coefficients and Matching Circuits for the 100 MHz and 60 MHz Devices

Device Designation	Operating Frequency (MHz)	Average Reflection Coefficient	Standard Deviation	Best Matching Circuit		Matching Circuit Used	
				Series (nH)	Parallel (pF)	Series (nH)	Parallel (pF)
100 MHz	96.8	0.2127-0.5887i	±0.0024+0.0073i	140	26	150	27
60 MHz	54.9	-0.2627-0.4798i	±0.0072+0.0430i	147	73.2	150	68

2.3.2 IDT Responses

Figure 17 shows the unmatched responses of both devices and compares it to the frequency response after the matching described in Section 2.3.1. The central frequency for the devices operation was found to be 96.8 MHz and 54.9 MHz for the 96 and 60 MHz devices respectively. Photoresist was applied to the edges and center of the 60 MHz device to absorb unwanted reflections and smooth the curve.
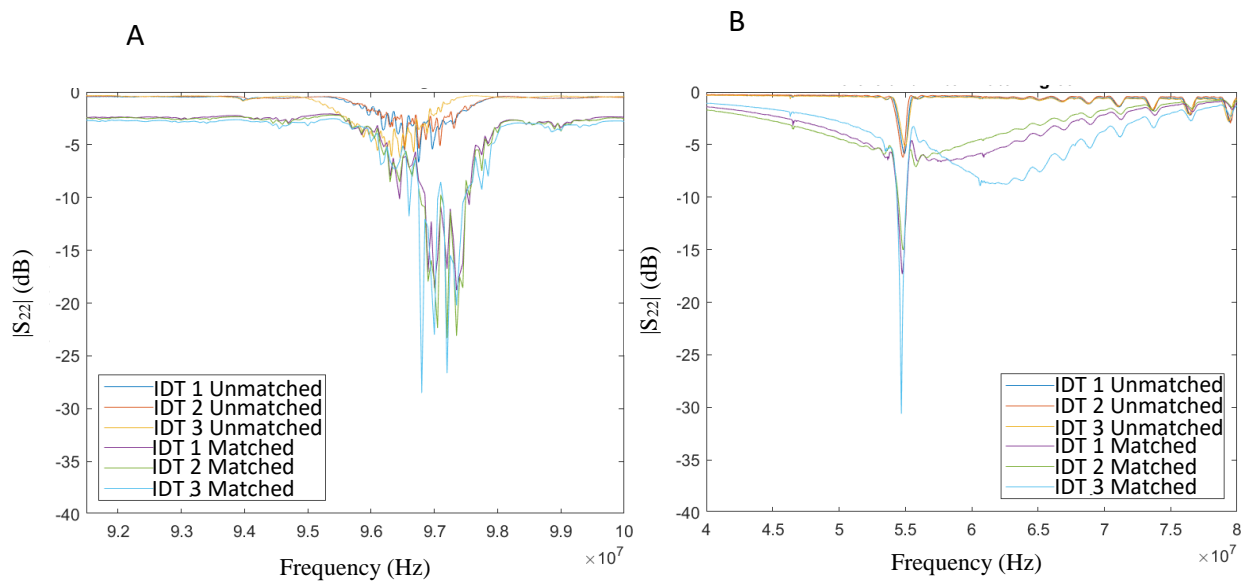
Figure 17. Signal improvement via matching. A) Unmatched and matched reflection coefficient ($|S_{22}|$) frequency response for IDTs at operating frequency around 96.8 MHz B) Unmatched and matched $|S_{22}|$ frequency response for IDTs at operating frequency around 54.9 MHz

Figure 18 shows the attenuation as a result of a 1 mm wall thickness PDMS microfluidic channel on the surface and a surface functionalization with a layer of Krytox 103 Oil. For the 100 MHz devices the drop at the operation frequency due to attenuation is -36 dB and -50 dB for the PDMS and Krytox respectively (Figure 18A). From the calculation described in Section 2.2.6 the drop is power from a 1 mm thick channel was predicted to be about 98.2%. The data in Figure 18 aligns closely with the theoretical giving a drop of 98.4%. For the 60 MHz device the resulting

23

drop at the operating frequency for the PDMS channel and oil liquid layer is approximately -18

dB and -48 dB respectively. The theoretical attenuation due to the PDMS channel at this

frequency was 83.2% and the measured was 87.4%. This difference is likely due to inconsistent

channel wall width. The decrease in frequency in the new SAW devices has, as expected,

successfully reduced the attenuation for the PDMS microfluidic channel. However, the

attenuation due to the liquid layer did not decrease.
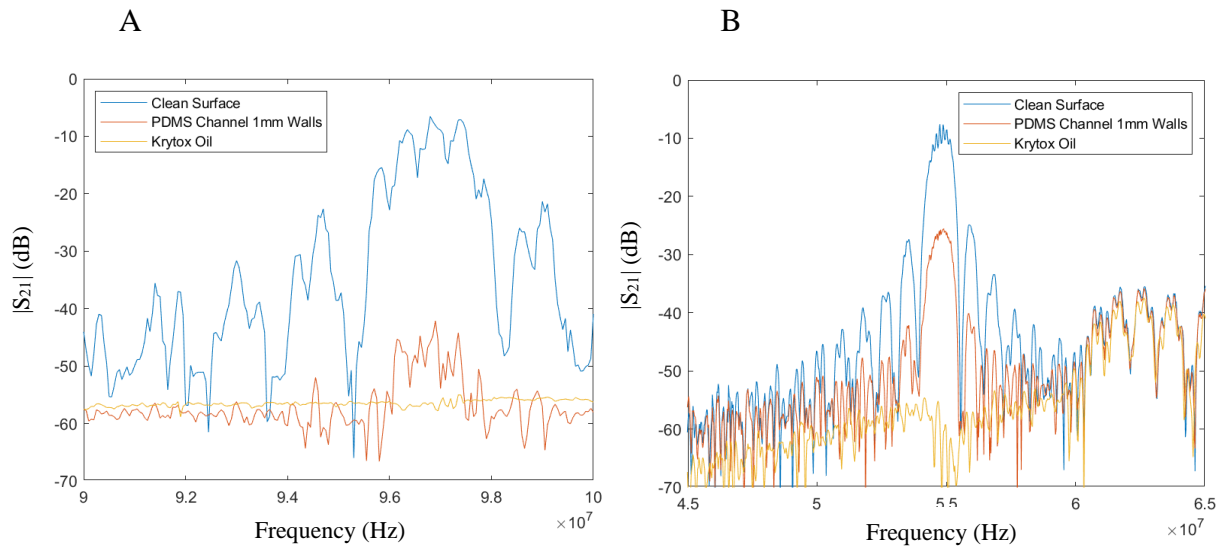
Figure 18. Attenuation due to surface structures A) on 100 MHz SAW devices. B)
Attenuation due to surface structures on 60 MHz SAW devices

2.3.3 Determining the Operation Frequency

Figure 19A shows the calculated acoustic force on a particle of diameter 100 nm in water

as a function of distance from a pressure node at various frequencies. Only one wavelength of

SSAW is plotted for each frequency, with three nodes and two antinodes present, similar to

Figure 5. This was done in order to determine the optimal frequency of operation. The plot

shows that due to attenuation the smallest amount of force is generated by the 96.8 MHz

frequency and the largest is around 60 MHz. Figure 19B shows the maximum time it takes for a

100 nm particle to migrate to a pressure node at a given frequency. The solvent properties in these calculation were those of water. The frequency at which the travel time is the smallest is about 60 MHz, confirming that 60 MHz is the optimal frequency.
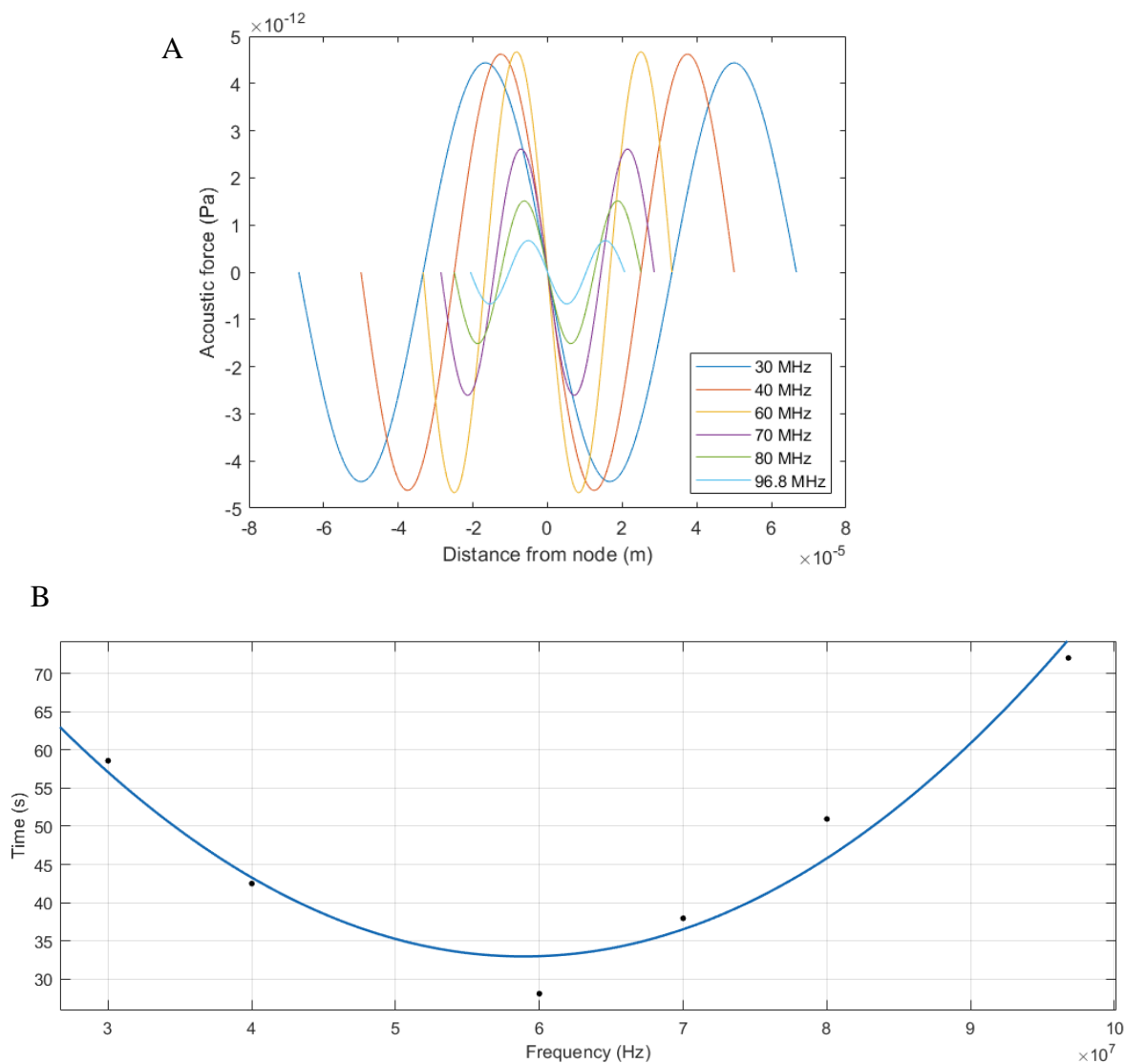
Figure 19. Determining the optimal operation frequency. A) Acoustic force as a function of distance for one SSAW wavelength from a pressure node at various frequencies taking into account attenuation, similar to Figure 5. B) Using the acoustic face data from A) the time it takes for all particles of 100 nm diameter to move to the pressure nodes. The points represent the calculated values at certain frequencies and the line is the best fit curve based on this data.

2.4 Discussion:

2.4.1 Effectiveness of SAW Devices and Setup

The pogo pin clip system resulted in consistent values of impedance. Figure 15 showed that the reflection coefficient measurments did not vary significantly for either 100 MHz or 60 MHz SAW devices, having standard deviations of ±0.0024+0.0073i and ±0.0072+0.0430i, respectively. The pogo pins also showed consistent performance regardless of the input port: with completely different pins at different ports providing a near identical responses (Figure 15). This demonstrates that the experimental setup provided a stable and consistent electrical connection and acts as a plausible alternative to wire bonding. It is important to keep in mind that all delicate pins need to make contact and be provided with appropriate pressure. Fine tuning the screws which push down on the pins is crucial for maintaining a proper connection without damaging the pins.

The measured operating frequencies of both the 100 MHz and 60 MHz devices were found to be 96.8 MHz and 54.9 MHz, respectively, both lower than their theoretical values. This is most likely due to the surface loading by the finite thickness electrodes used in the manufacturing of the IDTs. Chromium and gold are heavy metals are part of the load on the surface. An increase in the surface load will decrease the operation frequency. Also, the fabricated fingers were varied in width and some were only around 6 μm due to variation in exposure during the photolithography.

The matching circuits were determined by using the Smith chart to bring the impedance to the center of the chart (Appendix A). The capacitors and inductors selected had commercially available values as close to the calculated value as possible. There was variation in the impedance response between devices giving a range of quality in the matching as the average

impedance value was used for the circuit design. This was likely due to variations in the IDTs produced during photolithography. Even with both variations in the circuit component values and IDT fabrication, the impedance matching still provided an improvement in power transfer for all devices. As seen in Figure 17, the matching circuit provides drops in the reflection coefficients by anywhere between 9 and 25 dB, resulting in reflection coefficient values around -20 to -25 dB for the 100 MHz device, and -17 to -30 dB in the 60 MHz devices. Any value of $|S_{11}|$ greater than -10 dB would compromise the acoustic power transduced to the surface and should be better matched. The drops in these values below this threshold of -10 dB indicates that of power that reflected back to the signal generator is now being delivered to the fluidic system and impedance matching has been successfully achieved.

2.4.2 Surface Structures

The amount of attenuation from the 96.8 MHz delay lines due to the microfluidic devices and oils had the potential to affect the manipulation of the samples. A drop to -40 to -50 dB means that the wave was reduced to noise level before reaching the other IDT. Chapters 3 and 4 discuss in more detail the impact this has on the effectiveness of the particle and droplet manipulation. The overall result observed, however, was no movement from either the particles or droplets. One solution to this issue is to reduce the quantity of attenuating substances on the surface. The microfluidic channel walls can be reduced in thickness and the oil layer can be made thinner as well. Other materials could be considered for the channel. For example, glass, a common material for microfluidic channels, does not absorb acoustics as much but has an acoustic impedance around ten times higher than water[79]. This results in large amounts of the acoustic energy being reflected before entering the channel and the boundary between the two materials. Elastomeric materials, such as PDMS, are preferred over glass as they tend to have

acoustic impedances comparable to that of water reducing reflection[46]. On the other hand, elastomeric materials tend to absorb energy due to their viscosity which normally leads to higher attenuation than glass and crystals in general[80]. When selecting a material to use it is important to consider not only its acoustic properties but also its ease of use. For microfluidic devices a polymeric material like PDMS is often used due to it being air-permeable, which prevents bubbles, and having a low temperature bonding to devices[81]. Glass devices are also more fragile and prone to damage. Altering the material can only go so far however, as reducing the size of these structures can also diminish their effectiveness. Smaller channel walls were found to be prone to leaking and thinner liquid layers are prone to dewetting. Another solution is to reduce the operating frequency of the devices. This lead to the development of the 60 MHz IDTs. The attenuation from these devices is still substantial, about -18 dB, but is an improvement over the -36 dB drop from the 96.8 MHz devices. There also seems to be other modes in the frequency response. In Figure 19 there are smaller peaks around 60 to 65 MHz that are relatively unaffected by the channel or oil. These were most likely other wave modes that have higher penetration depth into the crystal and therefore do not interact with the top surface as much.

The frequency of 60 MHz was selected after determining what frequency would provide to optimal power shown in Figure 19. Without attenuation the amount of acoustic force would simply increase with frequency. However, it is clear that the addition of attenuation in Figure 19 the higher frequencies dampen the signal much too quickly. For this reason, 60 MHz was chosen as it would provide the best balance between the attenuation and acoustic force. Figure 19B confirms this as the particles in solution move the fastest around 60 MHz. Any higher and it attenuates too quickly, any lower and the wave is not delivering enough power. More viscous

solutions, such as blood, would increase the attenuation, but the optimal frequency would stay the same.

2.5 Conclusions

This chapter presented the analysis and design of the SAW devices and related electronic components used in this project. An alternative to wire bonding for an electrical contact system was developed using pogo pins. They allowed for a consistent electrical connection, while also allowing for easy plug and play functionality. Two delay lines were assessed: one designed to operate at 60 MHz and one at 100 MHz. It was found that the actual operating frequency for each device was lower at 54.9 and 96.8, respectively. Matching circuits were designed in order to minimize reflection of the IDTs. After adding the matching circuits the $|S_{11}|$ values dropped from around 9 to approximately 25 dB.

There were also significant attenuation from the structures and materials placed on the surface for microfluidic tests. The attenuation of the 100 MHz devices due to the PDMS microfluidic channel and the Krytox oil was found to be about -36 dB and -50 dB respectively. For the 60 MHz devices the respective losses were -18 dB and -42 dB. The 60 MHz devices were intended to maximize the amount of energy transferred to the microfluidic channel, and the contained particles, as that is the frequency calculated to achieve the best balance between acoustic force and attenuation.

CHAPTER 3:

SAW PARTICLE SEPARATION AND MICROFLUIDICS

3.1 Introduction

As discussed in Chapter 1, pancreatic cancer has one of the bleakest outlooks among cancer. According to the American Cancer Society, the five year survival rate for pancreatic cancer in the United States is around 10%[1]. This low survival rate is due mostly in part to the asymptomatic nature of the disease. For this reason screening is key. Current screening methods involve either imaging or blood tests looking for indicative biomarkers[4]. However both methods typically have low sensitivity and are better for monitoring than screening. Being able to better isolate biomarkers within the blood could substantially increase the sensitivity of these tests. This chapter discusses the groundwork for improving upon the current biomarker separation using SAW and microfluidic channels. The end goal is to use SAW to isolate exosomes and other biomarkers from the blood and concentrate them for more sensitive detection. This work focuses on producing a basic working SAW separation device, similar to the work done in Shi et al 2009[20], Destgeer et al 2013[34], and several others[42–44], using the SAW devices designed in Chapter 2. The
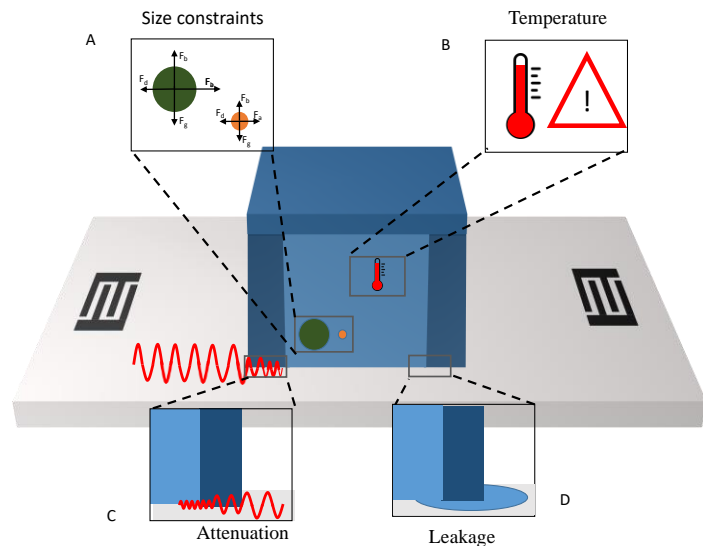
plays a large role in the amount of acoustic force exerted upon it. B) The fluid and channel heat up as the SAW is running and can damage heat sensitive particles in solution. C) The PDMS channel will heavily attenuate the SAW as it enters the system. D) Bonding PDMS to LiNbO3 is challenging and leakage may result.

challenges associated with that are shown in Figure 20. From there the possibilities of improving

upon its use for liquid biopsies will be explored.

3.2 Materials and methods

3.2.1 Microfluidic channels

The microfluidic channels were made from PDMS using soft photolithography at the

Zhang lab at Dartmouth. The channels (Figure 21) are 1.5 cm long, 0.4 cm wide, and tapered to a

0.08 cm point at both ends. The channel height is 40 µm. The channels were cut to size using a

scalpel, reducing the amount of excess PDMS to a minimum. The wall thickness at the area of

SAW actuation was cut to around 1 mm thick (Section 3.3.1). The walls outside of the SAW area

were kept thick to help with bonding.
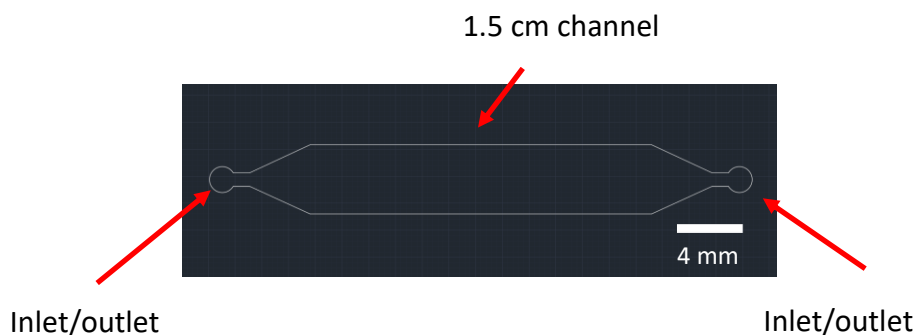
Figure 21. Microfluidic channel design

3.2.2 Plasma Bonding

A SAW device was first sonicated in warm acetone for 25 minutes followed by

isopropanol for 25 minutes to remove any photoresist. Then a prepared microfluidic channel and

the SAW devices were sonicated in isopropanol, ethanol, and then High Performance Liquid

Chromatography (HPLC) grade water for 5 minutes each. Both were then dried with nitrogen

and placed in a PE-25 Series Plasma Oven (Plasma Etch Inc.) for 30 seconds. The oxygen to air

ratio should be high and the cc/min of oxygen into the system was set to between 30 to 50 cc/min. A good indicator that the oxygen/air ratio was good for plasma treatment was a pale purple color filling the entirety of plasma oven space. Immediately after plasma treatment, the channel was placed on top of the SAW device surface at the desired location. It was then placed in a 60 °C oven with approximately 18 g of weight on top overnight. The next day the device was removed from the oven and silicone sealant is applied to the ends of the $LiNbO_3$ where the channel hangs over in order to prevent leaking from those areas. The sealant was allowed to harden in the oven for 20 minutes before running any liquid flow experiments.

3.2.3 Gold Etching

100 MHz SAW devices were coated in photoresist in the areas where the gold needed to be kept. The photoresist was allowed to dry for 10 minutes before the devices were dipped in gold etchant. The devices were allowed to soak in the etchant until all of the gold in the exposed regions was visibly removed. The samples were then soaked in chrome etchant until all the exposed underlying chrome layer was visibly removed. The devices were rinsed in DI water and then acetone to remove the photoresist. Figure 22 shows the area to be etched off. This process was conducted by George Bernhardt in the cleanroom of FIRST at UMaine.
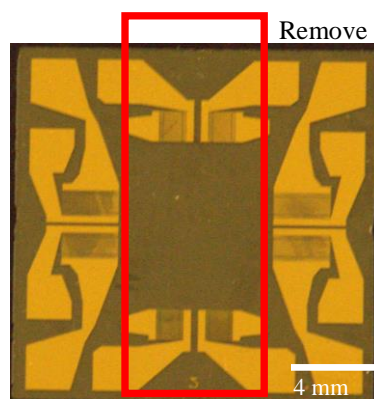
Figure 22: A 100 MHz SAW device before etching. The gold that needs to be removed is outlined.

3.2.4 Microfluidic Setup Adjustment

The microfluidic setup needed to be adjusted to work properly. First of all, in order to observe the particles within the channel they had to be placed under a microscope at 10x magnification. As seen clearly in Figure 23C the objective left little space for the microfluidic setup and required some careful space management in order to be able to view the samples without putting too much strain on the channel or the tubing and causing damage. In order to prevent this from happening, the channel was designed to be as long as possible (1.4 cm) without overhanging from the SAW device. Also the Tygon tubes were taped away from the objective and metal connectors were cut to be as short as possible.

The successfully bonded channel and SAW device were inserted into the circuit board as described in Chapter 1. One port was attached via coaxial cable to the RF signal generator system (Figure 23B). The board itself was taped down to the stage of the microscope. 1/16'' Tygon tubing with 0.025'' dimeter steel connectors were inserted into the holes of the channel. The tube at the feeding end was connected to a syringe inserted into a NE-1000 syringe pump (Figure 23A). The tubing at the outlet was inserted into a collection beaker. Samples run through the channel consisted of a 0.01% Tween80 solution with polystyrene microparticles of varying sizes. The sizes used were 20 μm, 12 μm, 10 μm, and 7 μm diameter. The syringe pump was operated at 20 μL per minute. During the initial startup of the pump the device and board was held vertically to push bubble up and out of the channel.
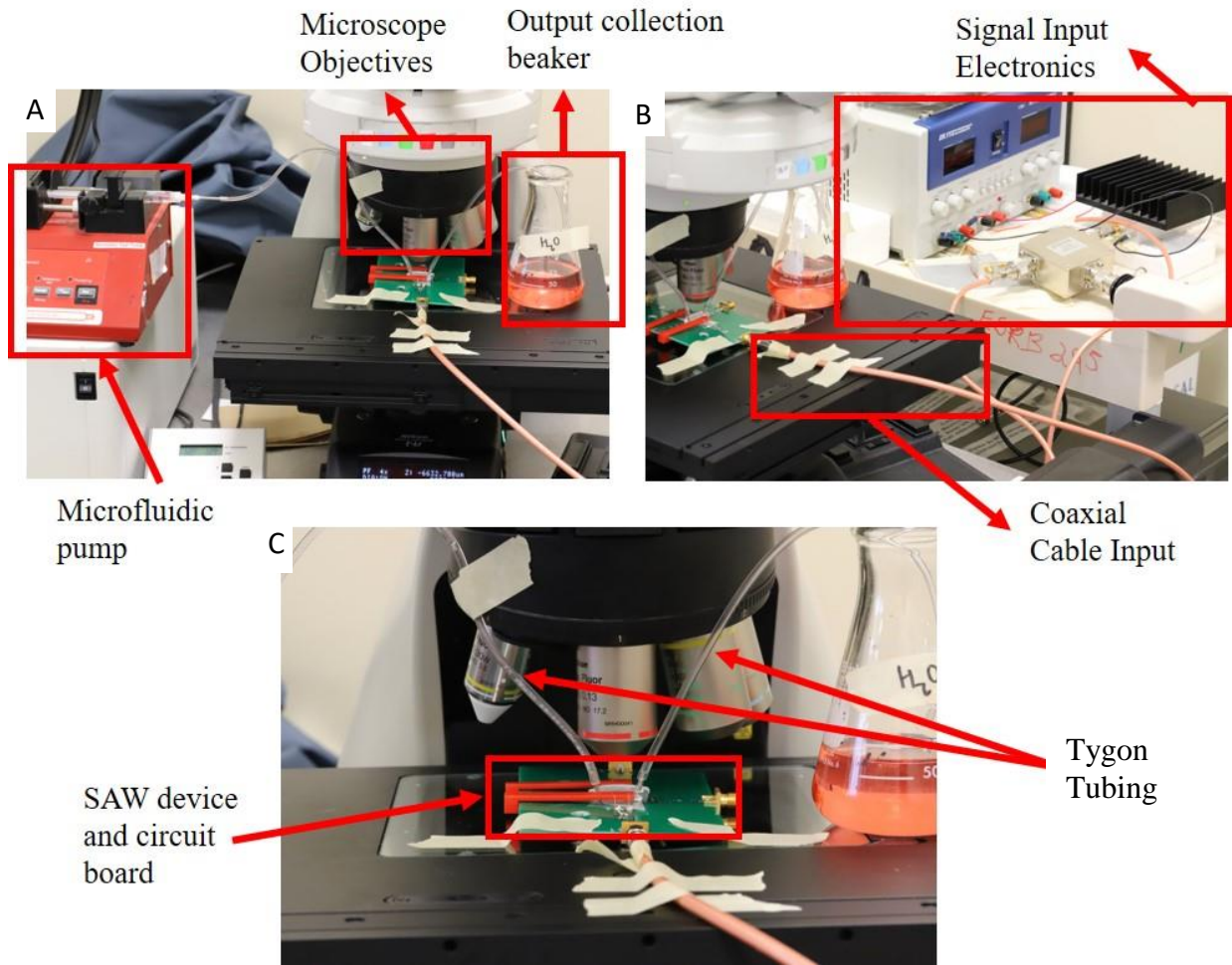
Figure 23. Microfluidic setup. A) The syringe pump is shown connected to the microfluidic channel with microscope objective and collection beaker. B) The signal generator and signal generation circuitry sending the RF signal to the SAW device via coaxial cable. C) A close up of the SAW device on the circuit board with microfluidic tubing leading into the channel and into a collection flask.

3.3 Results

3.3.1 Bonding of device to surface

Figure 24 shows a successfully bonded PDMS channel on top of a SAW device along with several points of common failures. After the oxygen/air ratio in the plasma oven was increased the bonding improved and the leaking problems decreased in frequency.
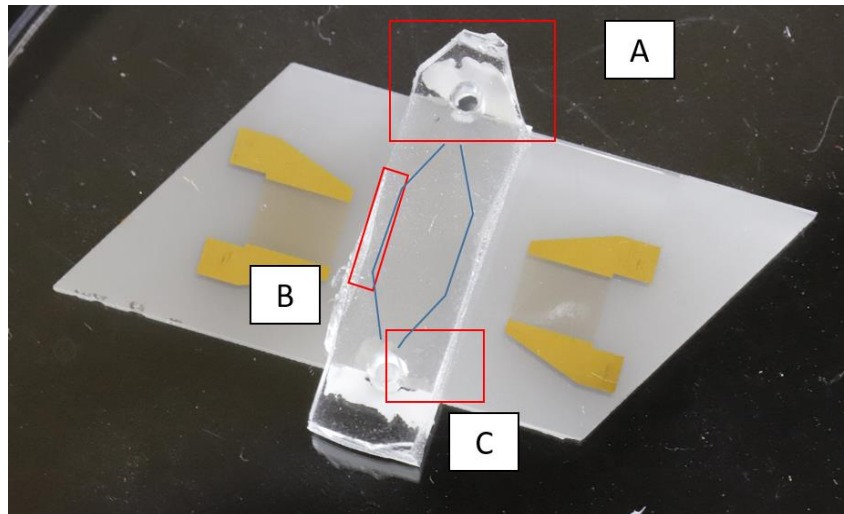
Figure 24. PDMS channel on top of 60 MHz SAW device. There are several critical points where issues occurred. A) The channel was slightly too long for the devices. Silicone sealant was applied to make sure nothing leaked from the ends. B) The channel itself needed to be placed in the center of the device with widest section in the path of the SAW. The thin walls were prone to leaking. C) Leaking commonly occurred at this spot. The water often flowed underneath the silicone sealant and leaked from the side. It was important to place some sealant up over the edge to prevent this.

Figure 25 shows the 100 MHz device before and after etching away some of the gold. Most of unwanted gold and chrome was removed with a few spots remaining. The PDMS channels were able to bond effectively to the newly etched surface.
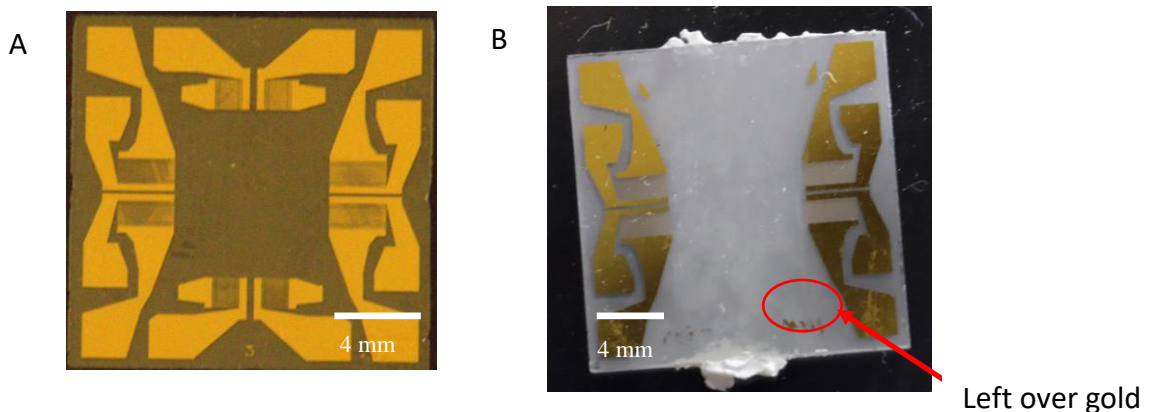
Figure 25. Etched SAW device. A) Before etching and B) after etching.

3.3.2 SAW Particle Separation

Figure 26 shows a set of time-lapse images of 20 μm diameter particles moving through a channel with the SAW on. The numerous spots in Figure 26A are the polystyrene particles moving through the channel. The particles moved quickly with little sticking. When the SAW was turned on the result was Figure 26B. The two spots in the figure are particles that have been zoomed in on. The particles move into the SAW area and immediately stop once there. Tapping on the channel with tweezers after turning the SAW off could get the particles moving again.
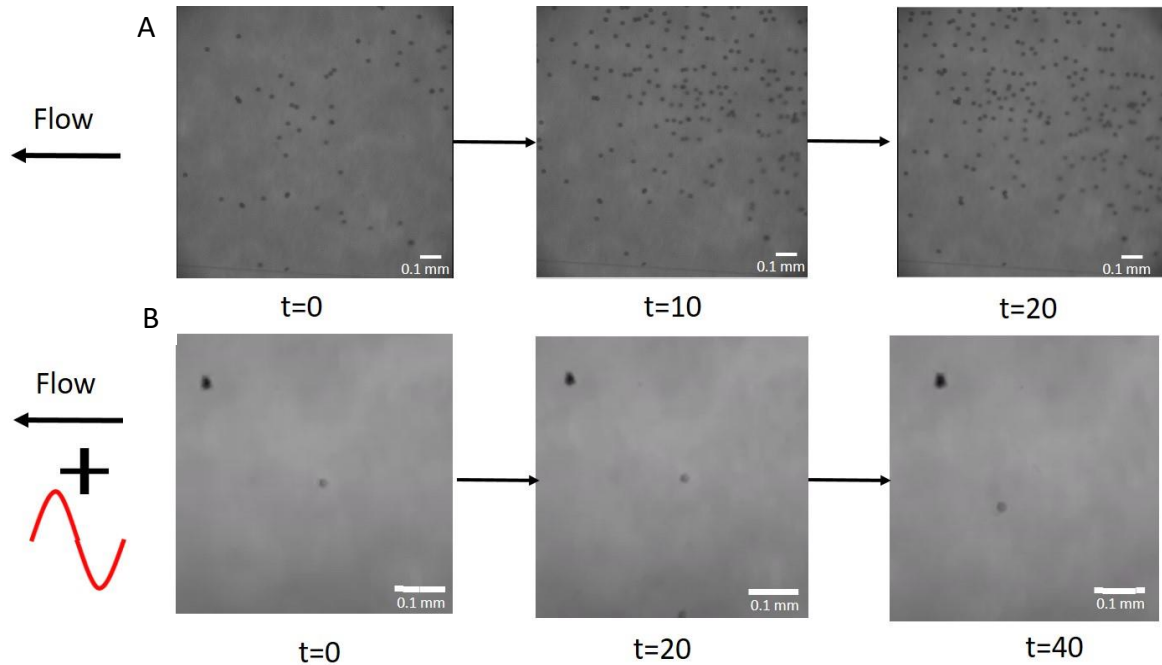
Figure 26. Particles flowing through channel. A) A high concentration of 20 μm diameter particles moving through the microfluidic channel with a 20 μL/min flow rate. B) A low concentration of 20 μm particles moving at the same flow rate.

Figure 27 shows an air bubble that was consistently present in the corners of the PDMS channel. The bubbles formed at the channel edges. The result of air getting trapped during filling the channel interfered with the separation of the particles. When the SAW

was turned on the bubbles formed what is seen in Figure 27. The area of the air bubble

began to increase and droplets of fluid began to form within this bubble area. The SAW

was most likely vaporizing the fluid allowing the air bubble to expand, and causing

droplets to condense on the ceiling of the channel.
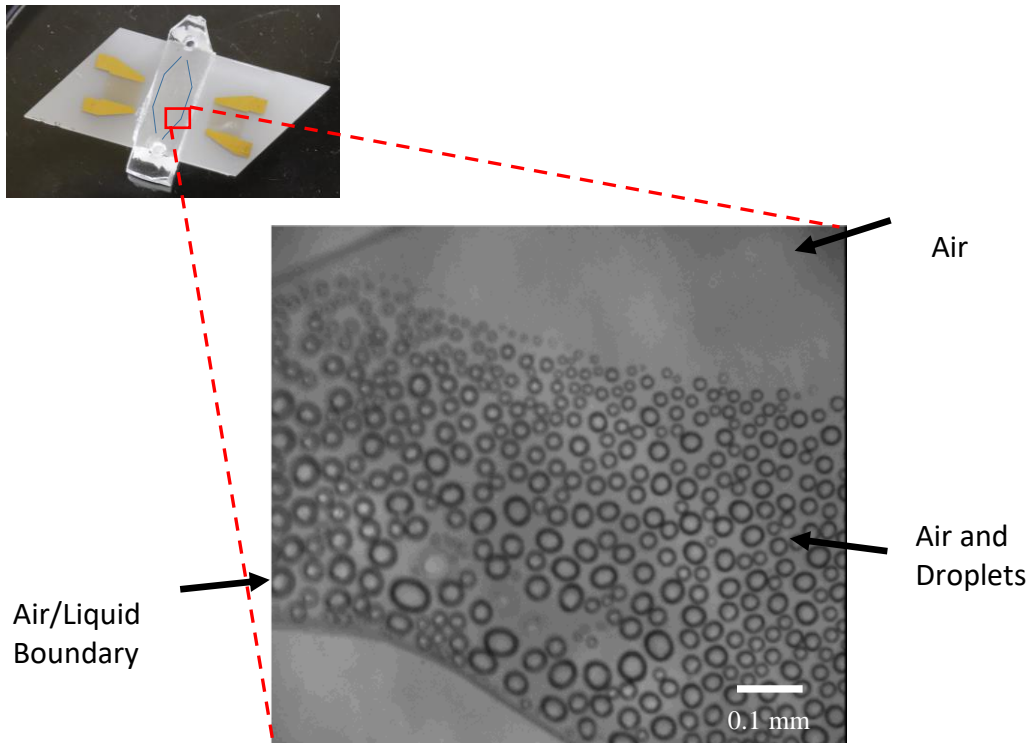
Figure 27. Bubble inside the corner of the channel at 10x magnification. With the SAW running beads of water form on the ceiling of the channel forming the structure above.

3.4 Discussion

3.4.1 Bonding Challenges and Solutions

Bonding a PDMS microfluidic channel to a LiNbO$_3$ SAW device presented quite a few

challenges. First of all the PDMS does not bind as well to LiNbO$_3$ as it does to other commonly

used substrates, such as glass. The system is prone to leaking at the points shown in Figure 24,

and/or simply falling off. This signifies that the bond is not covalent and something was

preventing a strong bond. This is likely due to the pyroelectric nature of the substrate allowing

37

dust and debris to easily stick. It is certainly possible to plasma bond to lithium niobate as it has been done many times in the literature[20,34,35,44]. After making a stricter cleaning procedure and adjusting the plasma concentration, based off of the literature, a more consistent protocol was determined. The surface must be kept as clean and as unmarked as possible. Having minimal contact with tweezers and no contact with hands or gloves is a must. Nothing should touch the surface of the device. When switching solvents or moving the device it should be covered and exposed to the air for as little time as possible. Dust and debris from the air can easily stick to the surface of the $LiNbO_3$ as it is pyroelectric and is charged. Another very important factor was the ratio of oxygen to air in the plasma oven. If it is too low the surface will not be properly prepared and bonding was difficult. For successful bonding the cc/min of oxygen into the oven was set to around 30 cc/min giving a pale purple color.

We were able to bond the PDMS to the $LiNbO_3$ but it was not possible to easily bond to gold simultaneously. The 100 MHz devices had IDTs all around the edges of the device. In order to bond a channel to the surface without leaking there either had to be a bond to the gold or the gold had to be removed. Using adhesives in conjunction with plasma bonding proved difficult as they either heavily attenuated the wave or prevented good contact between the PDMS and $LiNbO_3$ during plasma treatment. There are chemical treatments that would allow for gold to bind to PDMS but would compromise the surface bonding to $LiNbO_3$[82]. It was much simpler to just remove the unwanted metal and plasma bond. The removal of the metal was not perfect in some cases. For unknown reasons a few spots of gold and chrome would not be dissolved in the etchant no matter hold long we soaked it. These spots were small enough to be deemed insignificant and largely ignored. The new devices operating at 60 MHz (Figure 11B) were

designed so that there was no gold in the way of the channel and so the etching was not necessary.

3.4.2 Separation of Microparticles

With the setup and device completed the next step was to test whether the SAW could push particles within the channel. When particles of 20 μm diameter were run through the channel they were clearly visible with the 10x objective (Figure 25A). However, due to their hydrophobicity they tended to stick to the tubes and channel[83]. A small concentration of surfactant (Tween 80) was used to prevent clumping and sticking to an extent. An alternative would be to oxidize the PDMS surface prior to plasma bonding with something like piranha solution[84]. When the SAW was turned on, shown in Figure 26B, the particles stopped within the channel. Jostling the channel could dislodge them but they would immediately stick to the channel again. What was likely happening was that the SAW was pushing the particles towards the ceiling of the channel where they stick. There it stuck to the PDMS until dislodged. Gijs et al. 2004 shows a similar problem with their magnetic beads. The surfactant in the solution should help to mitigate this problem, however further runs with the new 60 MHz SAW devices have yet to be conducted.

Another issue that was encountered while running the SAW was the presence of air bubbles. These were caused by incomplete filling of the channel. This was a common occurrence in this system and there are several solutions to prevent this, including adjusting the shape of the channel, increasing the wettability, and lowering the flow rate. When the SAW was turned on the fluid in the solution was likely vaporizing and creating condensation on the ceiling of the channel within the bubble (Figure 27). Therefore, like in most microfluidic systems, it is important to removing the air bubbles in the system by allowing the channel to initially fill from

a vertical position. An oxidation step to increase the inner wettability may also help more easily fill the channel and push out air.

3.5 Conclusions

In this chapter we have discussed how a complete microfluidic and SAW setup has been made using both the 100 MHz and 60 MHz devices. Bonding problems due to excess gold on the 100 MHz device and imperfect plasma treatment were solved using metal etching and a higher oxygen/air ratio than normal, respectively. The polystyrene particles introduced were found to be affected by the SAW but movement and separation similar to that of works such as Shi et al. 2009[20,44] and Destgeer et. al 2013[34] was not yet achieved. Mostly the particles have stuck to the tubing and the top of the channel when the SAW was active due to hydrophobic interactions. The SAW was pushing the particles around the channel and they were sticking to the top of the channel. A surfactant was added to prevent this and appears to prevent sticking to the tube but its effect on the sticking to the PDMS channel has yet to be determined. Improving of this separation setup is the next step for this aspect of the project. One thing that is clear however, is that microfluidic devices add a level of complexity to the system and issues as discussed above. Perhaps avoiding using them entirely would eliminate the issues. The exploration of open microfluidic systems for liquid biopsy analysis is explored in the next chapter.

CHAPTER 4:

SURFACE FUNCTIONALIZATION AND MICRODROPLETS

4.1 Introduction

As discussed in Chapter 1, there are many applications with small droplets that are possible using SAW. Everything from mixing[47,85–87], splitting[6,13,33,73], moving[47,86], evaporation[6,47,85], and aerosol production are possible[28,62,72]. Of particular interest in this work is SAWs ability to both move and concentrate droplets on the surface. In this chapter we will discuss the effectiveness of the SAW devices introduced in previous chapters to manipulate microdroplets on the surface. In the previous chapter it was shown that microfluidic channels are prone to many issues. With open microfluidics it should be possible to eliminate many of the issues such as leaking and sticking. Other methods of droplet manipulation include pressure[10], which requires some sort of microfluidic channel, or electric[10,88,89] and magnetic fields[10,88,90], which require charged or magnetic properties of the samples or the surrounding liquid layers[88]. SAW on the other hand does not require any channel walls or special fluid properties. Well placed arrays of IDTs and tracks of hydrophobic surface treatment can eliminate the need for closed channels[47]. On top of that, a chip featuring arrays of IDTs serving different functions could be created to perform multiple function, such as splitting and mixing, before and after the movement and concentration. This widely expands the possibilities and power of the system. This is not without its limitations however. The surface must be prepared in a way to facilitate movement. In the literature it has been done with thick, highly attenuating oil layers[86] or no oil layer at all[47,91], which could leave contaminants and residue on the surface[86].

There are many advantages to a liquid layer. Liquid layers or liquid-infused surfaces are an incredible tool in the area of material science. Liquid-infused surfaces have a thin layer of

liquid, in this case oil, trapped on the surface through chemical and physical forces[65,88,89,92]. This allows for hydroplaning creating a slippery surface and preventing sticking. For this reason it is great in antifouling applications[88,92]. When a droplet is placed on a liquid-infused surface the liquid will create a wetting ridge and a wrapping layer[93,94]. The wetting ridge is a buildup of fluid at the interface of the droplet and liquid layer. The wrapping layer is a layer of liquid that encapsulates the droplet. With these structures the droplet is protected from both the underlying surface as well as the surrounding environment. Evaporation is greatly reduced as a result[93].

This chapter discusses a system of droplet manipulation using SAW involving surface functionalization using a fluorinated oil/liquid layer and self-assembled silane monolayer. This functionalization is quick to apply, repair, permanent, and uses oil layers only 11 to 16 μm thick to produce a hydrophobic surface capable of facilitating microdroplet movement. This combined with a Peltier heating unit shows the systems capability of manipulating droplets at will and then controlling the concentration of the droplet to enhance further analysis.

4.2 Materials and methods

4.2.1 Surface Functionalization

LiNbO$_3$ SAW devices were functionalized with a monolayer of trichloro(1H,1H,2H,2H-perfluorooctyl)silane. A generic silane monolayer is depicted in Figure 28. The devices were first sonicated in isopropanol for 45 minutes and then dried with Nitrogen. After that the samples were oxygen plasma treated in a PE-25 Series Plasma Oven for 60 seconds. A solution of 100 μM silane in anhydrous toluene was prepared and the devices were placed in it overnight, allowing the silane monolayer to self-assemble. The next day the devices were washed with large amounts of anhydrous toluene and placed in an oven at 110 °C for one hour. Liquid layers were then formed with either Krytox 103 or Krytox 105 oil. One of these was dropped on the surface

and spread around using a 10 μL water droplet. These have viscosities of 30 cSt and 160 cSt respectively. The devices were set on their sides and drained for the 40 minutes[95].
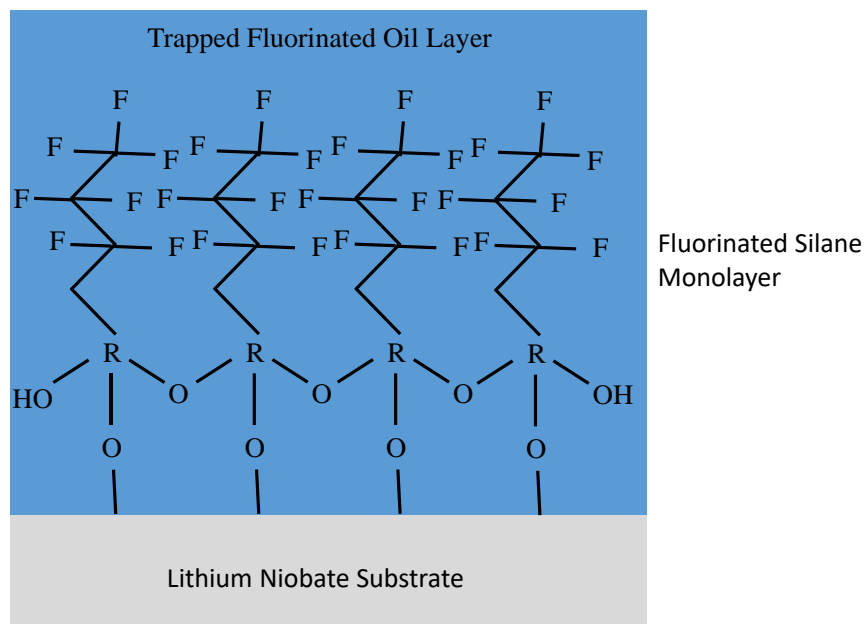
Figure 28. Functionalized oil layer diagram. The silane attaches to exposed oxygen on the surface of the LiNbO$_3$ and forms a monolayer. The fluorinated side chains trap a thin layer of fluorinated oil on the surface. Silane drawn is a generic structure for a fluorinated silane. The silane used was trichloro(1H,1H,2H,2H-perfluorooctyl)silane which has longer fluorinated functional groups than shown in the figure.

4.2.2 Determining Oil Layer Thickness

Pieces of LiNbO$_3$ were weighed and then functionalized with silane. A volume of 20 μL of perfluoropolyether (Krytox 103, Dupont) oil was applied to the surface and spread via the method in Section 4.2.1 and the weight was measured again. Using the density of the oil (192 g/mL), the area of the piece, and the mass change, the oil layer thickness was calculated. The pieces of material were then placed vertically for 10 minutes to allow excess oil to drain off. Then the pieces were weighed again to determine the new thickness. The sample sheen was examined by taking videos of the functionalized chip being rotated a various angles. Pools of oil and areas of dewetting were visible in this way. The draining, weighing, and sheen observations

were repeated until the change in the amount of oil became less than 1 mg for each sample. The final thickness was determined to be the target oil layer thickness for subsequent experiments.

4.2.3 Contact Angle

Contact angle was taken at various points in the functionalization process to confirm it was working. Samples were placed on a pedestal with a black background and a 20 μL droplet of water was placed on the surface. Using a CANON EOS 6D Mark II camera with a 100mm Marco Lens placed parallel to the device, photos of the droplet on the surface were taken. The contact angle plugin in ImageJ was then used to determine the contact angle of each droplet.

4.2.4 Tilt Angle

Tilt angle, or the angle at which a droplet on the surface starts to move due to gravity, was determined using a tilt stage setup with a digital level. Samples were placed on a glass slide which was taped to the tilt stage along with the magnetic digital level. The sample was tilted manually and recorded with a CANON EOS 6D Mark II camera with a 100mm Marco Lens. The exact moment of movement was determined using ImageJ and the angle on the digital level was recorded.

4.2.5 Droplet Concentration

In order to determine how much control over the evaporation of the droplet this functionalized surface would allow, droplets on the surface of a SAW device were concentrated using a Peltier heating device. The surface was heated to around 60°C, evaporating the droplets. To determine the concentration of a droplet, pictures were taken of droplets with rhodamine-G6 dye at concentrations ranging from 0.625 mM to 5.00 mM. ImageJ was then used to greyscale the images and determine a mean pixel value that would correspond to a given concentration. A standard curve was generated and can be seen in Figure 29. The effectiveness of evaporation was

measured by placing 20 µL water dyed of 1.25 mM rhodamine-G6 on the surface of the devices

and heated. Every ten minutes a photo was taken of the droplet and ImageJ was then used to

determine the concentration based on the standard curve.
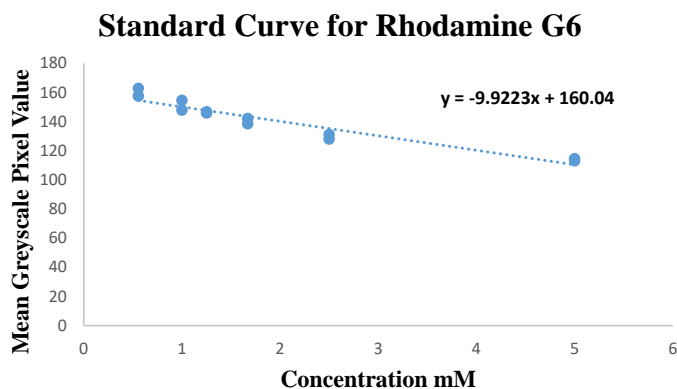
Figure 29. Standard curve of rhodamine-G6 dye vs. the mean grey pixel value.

4.3 Results

4.3.1 Functionalization

Figure 30 shows images of the Lithium Niobate before functionalization, after

functionalization, and after the addition of Krytox 103 oil. It was expected that the surface would

be uniform during each stage of the functionalization process. The surface looks smooth after

cleaning but appears non-uniform or blotchy after functionalization.
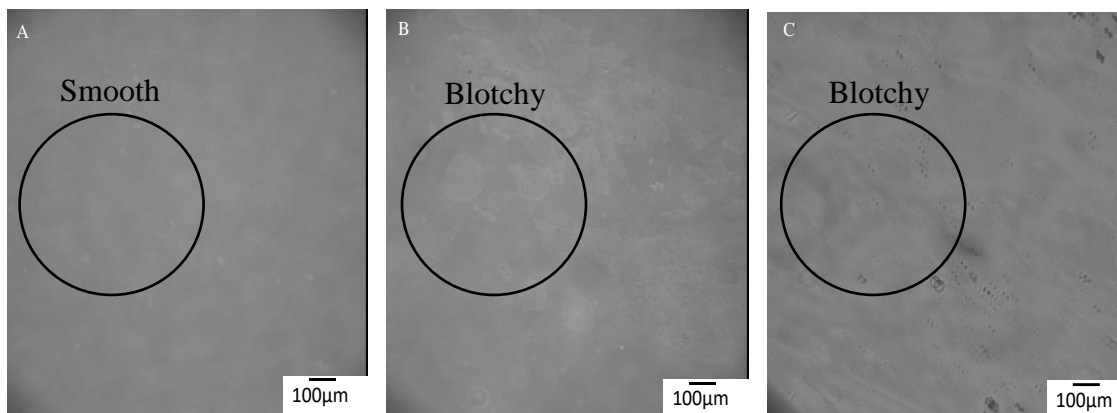
Figure 30. Surface microscope images of LiNbO$_3$ at various stages of the functionalization process. A) After cleaning with Isopropanol, B) after functionalization with silane, and C) after adding a 15 µm layer of Krytox 103 oil.

Figure 31 shows contact angle photos for a cleaned and functionalized Lithium Niobate chip. The contact angle for the clean chip surface was found to be 22±4.39° while the contact angle for the functionalized surface was 105.6±3.76 °.
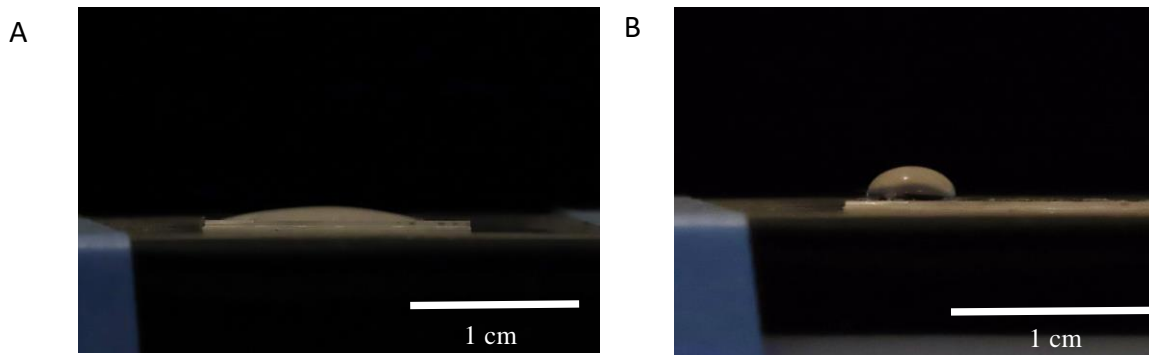
Figure 31. Contact angle before and after functionalization. 20 μL droplets used for contact angle measurements on the surface of a (A) cleaned and (B) functionalized piece of lithium niobate.

Figure 32 shows the results of running a tilt angle experiment on functionalized and non-functionalized chips with and without two types of Krytox oil (103 and 105). It was expected that the droplets would have a low tilt angle with oil and functionalization monolayer and high tilt angles without one or the other. The droplet on the functionalized chip without oil stuck to the surface and did not move even past the 90 ° point. When the 103 Krytox was added the droplet began to move at an angle of 2.3±1.3° with a silane monolayer and over 90 ° without it. For the Krytox 105 the tilt angle decreased to an angle of 1.7±0.47° with functionalization and stayed the same at over 90 ° without it. These values were taken with an oil layer that had not been drained. Thinner oil layers, using Krytox 103, measuring 8.34 and 12.4 μm thick showed tilt angles of 4.5±0.92° and 3.7±0.81° respectively. These are still low but higher than the values for the undrained layer.
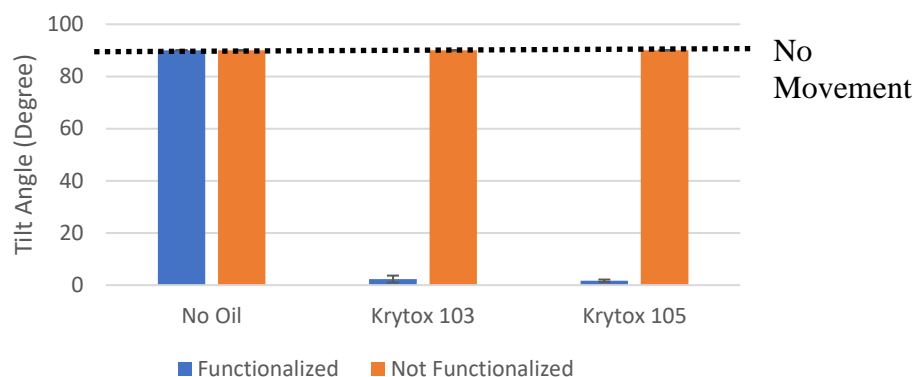
Figure 32. Tilt angle measurements. Both for functionalized and non-functionalized Lithium Niobate chips with and without Krytox oil. If a droplet did not slide on the surface it was given a value of 90 °, which was the largest angle the tilt stage could accommodate.

4.3.2 Oil Layer Thickness

An experiment was designed in order to determine the minimum thickness of a Krytox 103 achievable through draining. Table 2 shows the surface area and mass measurements of the pieces of $LiNbO_3$ used to determine the oil layer thickness. It was expected that layer thickness would decrease over time and level off to a minimum layer thickness. Which is confirmed by Table 2 and Figure 33.

Table 2: Measurements of Oil Layer Thickness

Chip	Surface Area (cm^2)	Initial Weight (mg)	Weight (mg) 0 min	Weight (mg) 10 min	Weight (mg) 20 min	Weight (mg) 30 min	Weight (mg) 40 min	Tilt Angle (°)
D1	1.25	313.2	330.8	320.1	317.6	316.1	316.0	4.4
F2	1.29	338.3	357.2	355.4	354.2	353.8	354.2	9.5
D2	0.756	188.8	198.5	194.0	192.0	191.7	191.5	4.2
F2	0.874	218.7	227.4	227.2	226.9	226.1	225.3	2.3
D3	0.995	268.1	294.7	276.1	274.9	272.4	271.4	3.4
F3	1.37	355.0	379.4	375.7	375.9	375.1	374.4	2.2

Figure 33 shows the change in the oil layer thickness as the draining time increases. Half of the

samples (blue points) were placed vertically and half were placed horizontally (red points)

during this time. The initial oil layer thickness was dependent on the size of the chip. The chips

that were placed vertically had final oil layer thicknesses of 15.7±3.19 μm. Chips left

horizontally had little change to their original oil layer thickness. Further draining of the device

only yielded changes in mass of < 1 mg. This loss can be attributed to evaporation and removal

during spreading with a droplet as control chips that were laid horizontal showed similar sized

fluctuations in mass. This confirms the earlier hypothesis that the oil would drain to an

asymptotic minimum value.
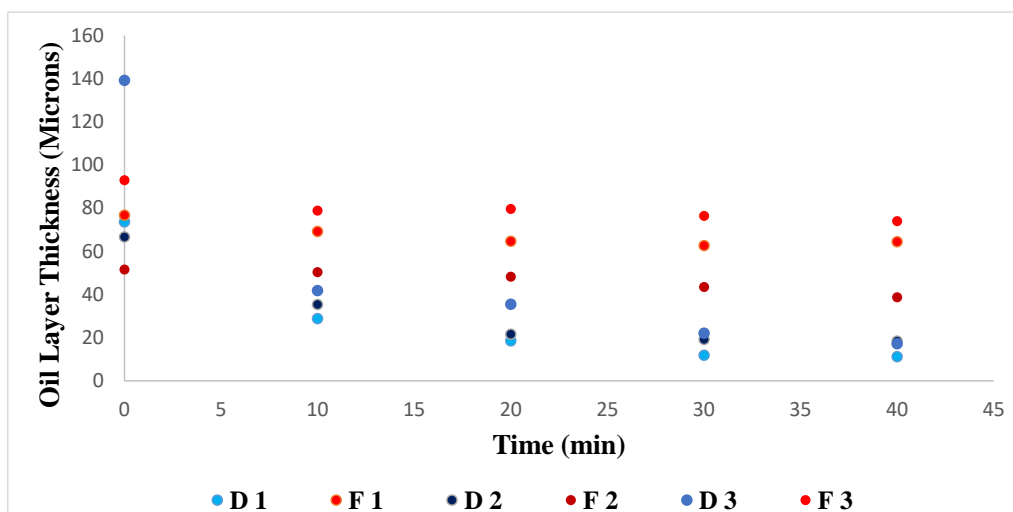
Figure 33. Oil layer thickness over time. Three LiNbO$_3$ chips were tilted vertically to drain while three were left horizontal as a control. Blue points represent drained samples while red points represent samples kept horizontal.

In order to examine the integrity of the liquid (oil) layers the sheen of the surfaces at various time

points was observed. If the liquid layer is stable, then one expects to see a continuous, uniform

surface. If one has an imperfect functionalized, the surface would dewet and show puddling of

the liquid over time. Due to the blotchiness seen in Figure 30 it was expected that dewetting

would occur on all samples. Figure 34 shows images of the pieces of LiNbO$_3$ tilted so that the sheen of the oil is visible. For all samples the oil appears to have pooled at varying locations indicating an unstable liquid layer.
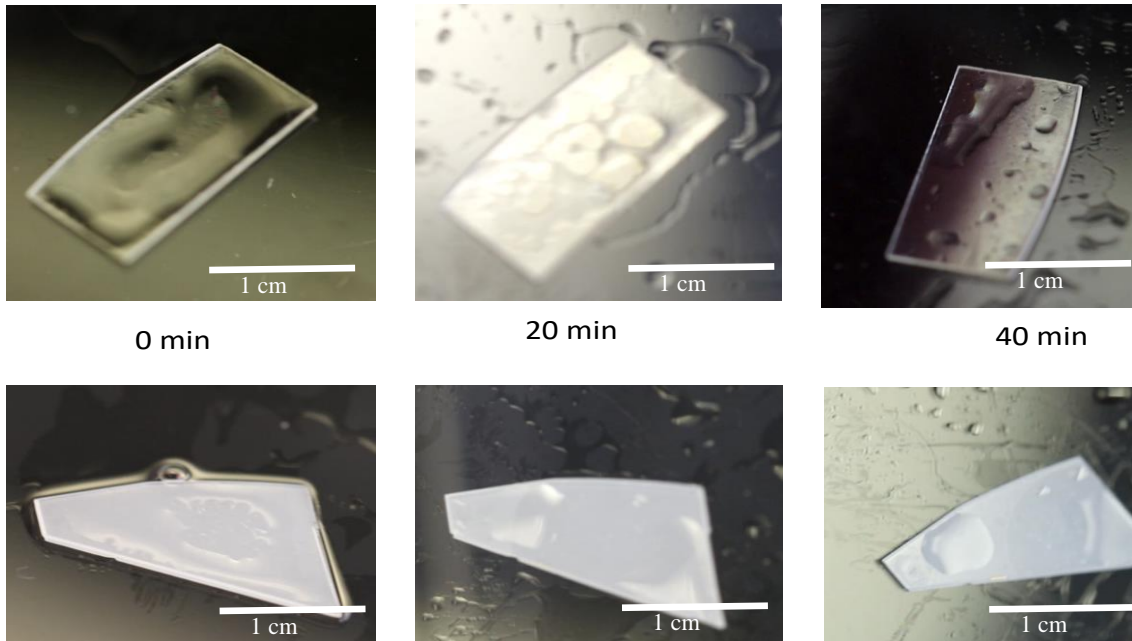
Figure 34. Sheen from LiNbO$_3$ chip dewetting. The images shown above were taken at 0 min, 20 min, and 40 min. The top set is from a chip that was drained and the bottom is from one that was not. Dewetting was observed on both. The oil used was Krytox 103

4.3.3 Droplet Manipulation

The liquid layer on top of the device is viscous and absorbs energy from the acoustic waves. In order to determine the amount of energy lost to the oil the transmission coefficient $|S_{21}|$ was measured for 100 MHz devices after functionalization, application of oil (Krytox 103), cleaning with a known solvent of the oil, and reapplication of oil after cleaning (Figure 35). It was expected that the S$_{21}$ values would drop significantly due to the oil. The sample was cleaned with NOVAC solution and tested to determine if removing the oil to apply a different one would compromise the surface properties. The oil dropped the signal by about -30 dB indicating severe

acoustic absorption before reaching the other IDT. When cleaned, the signal jumped up to

around -20 dB, higher than the original signal, indicating that the NOVAC had affected the

silane monolayer, changing the properties of the surface. When oil was reapplied the signal

dropped back down by -30 dB to noise level but was a fundamentally different curve. This

indicated a permanent change caused by the NOCAC washing.
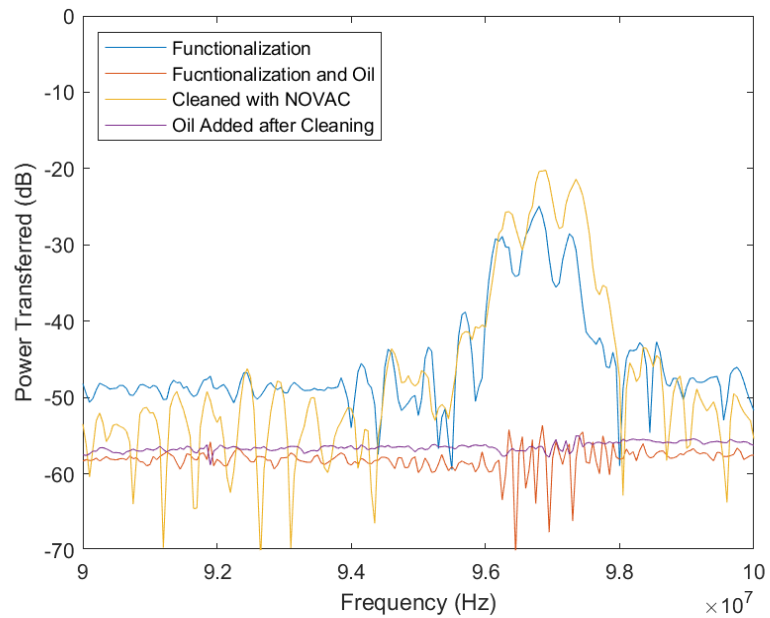
Figure 35. 100 MHz oil attenuation. Comparison of the SAW signal from the 100 MHz
devices after functionalization, addition of Krytox 103, cleaning with NOVAC, and addition
of Krytox 103 after cleaning.

As discussed in Section 2.3.2 (Figure 18B) this attenuation analysis was repeated with the

60 MHz devices without the NOVAC cleaning step (Figure 36). In this experiment a single SAW

device functionalized with a liquid layer had the oil drained for 40 minutes to create a layer

around 15 μm thick. It was expected that the attenuation would be less due to the lower operation

frequency. The peak at 54.9 MHz more than 60 dB in magnitude indicated that all of the power

was transferred to the oil before reaching the other IDT. There are other peaks at higher

frequencies that did not change very much. These are most likely plate modes, which due to

their higher penetration depth into the substrate are less effected by attenuation from objects on the surface.
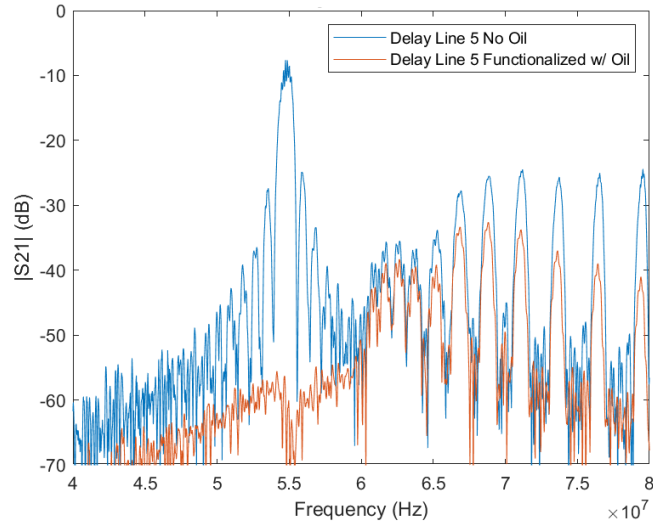
Figure 36. 60 MHz oil attenuation. The S_{21} measurements for a 60 MHz device with and without a functionalized oil layer. There was a large drop in signal at the operation frequency of 54.9 MHz and a lesser drop at peaks at higher frequencies.

In order to determine how effective the liquid layer (Krytox 103 oil layer) SAW device was at moving water droplets 10 μL droplets of water were placed on a SAW device at each point of the functionalization process. Figure 37 shows how the droplets responded on a surface cleaned with alcohol, a surface with a silane monolayer, a dewetted surface, and an even liquid layer surface. The droplet should only move on the evenly distributed liquid layer and deform or burst on the others. The cleaned surface yielded droplet elongation and spreading out along the surface. With a silane monolayer the droplet elongated but did not spread on the surface. When the oil layer was freshly applied the droplet moved in the direction of SAW propagation. After repeated use the oil layer had dewetted and the droplet simply deformed but did not elongate. A quick

respreading of the oil with a droplet restored the setup without any observable loss in

performance.
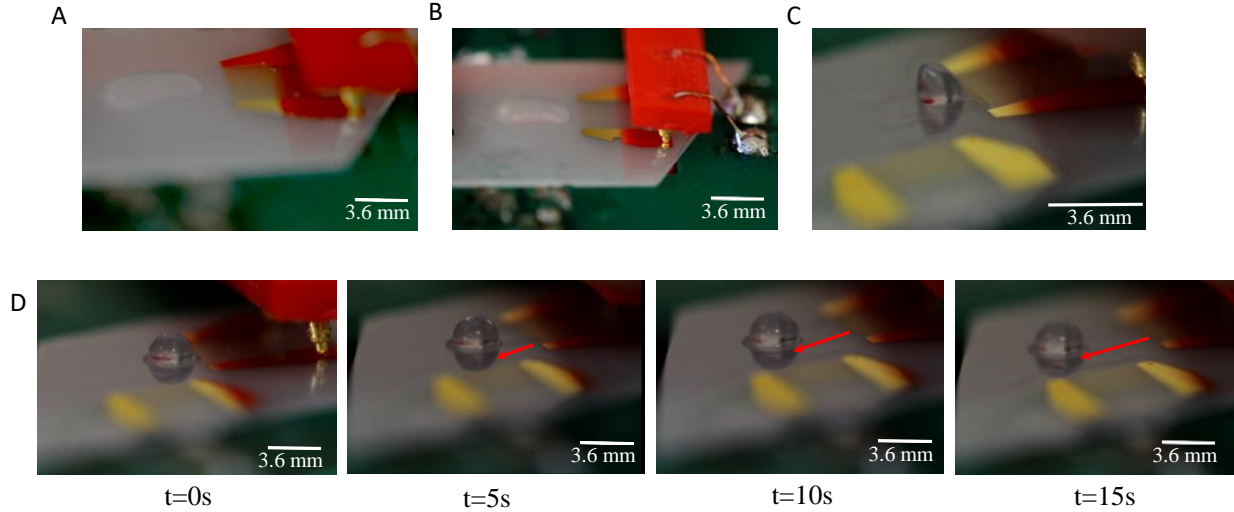
Figure 37. Droplet response to the 60 MHz SAW operated at 54.9 MHz. Response of a 10 µL droplet of water on a A) cleaned surface, B) silane monolayer, C) dewetted surface, and D) the droplet moving along a silane monolayer with an even 12.4 µm thick oil layer.

Table 3 shows the results of measuring the droplet movement speed while varying the oil layer

thickness and droplet size. This was done in order to determine the optimal parameters for

running the device. The thinner the oil layer and the smaller the drople,t the faster the droplet

moved. Figure 38 shows these data in column graph form. The standard deviations are large

especially for the 17.92 µm oil layer, likely due to the droplet moving backwards or to the side at

times or stopping completely as discussed in greater depth in Section 4.4.

Table 3: Droplet Velocity Based on Oil Layer Thickness and Droplet Size

Oil Layer thickness (µm)	Droplet Size (µL)	Average Speed (mm/s)	Standard Deviation
27.3	5	0.08	0.02
	10	0.07	0.05
17.92	5	0.28	0.25
	10	0.21	0.14
8.34	5	0.45	0.11
	10	0.28	0.07
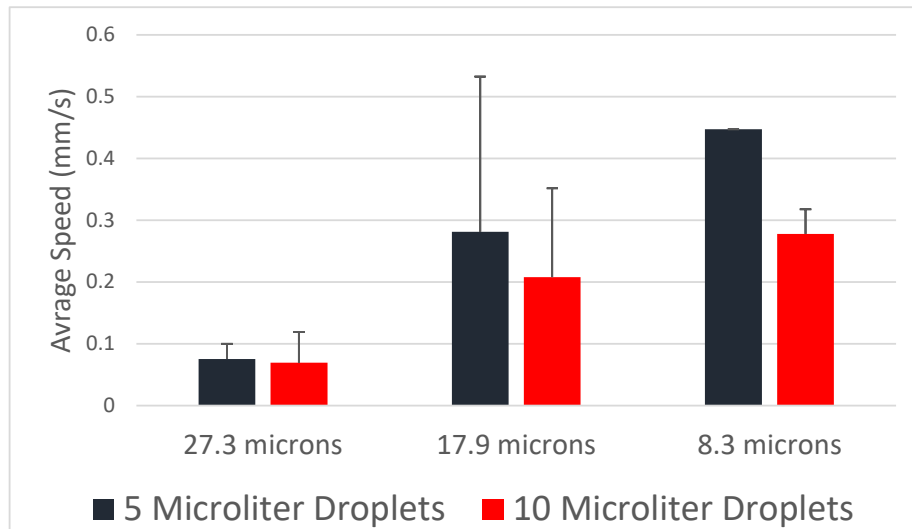
Figure 38. The droplet speed vs. the oil layer thickness and droplet size. The oil layer varied in thickness from 27.3 μm to 8.34 μm. Red bars indicate 10 μL droplets while black bars indicate 5 μL dropelts.

4.3.4 Droplet Concentration

Determining how well the evaporation and concentration of the droplets on a liquid layer could be controlled was done with the Peltier heating device setup described in Section 4.2.5, on a functionalized surface with a Krytox 103 liquid layer. Figure 39A shows the droplets of water with rhodamine dye as they were heated at 60 °C and evaporated. Figure 39B shows the final droplet diameter after complete evaporation had occurred. Without functionalization and oil the droplet created rings and the final diameter was comparable to the initial diameter. With fluorinated oil (with and without a silane layer) the droplets were effectively concentrated from 1 μM to 4.2±0.52 μM. However, without an underlying silane monolayer the variation in droplet size increased (Figure 39B).
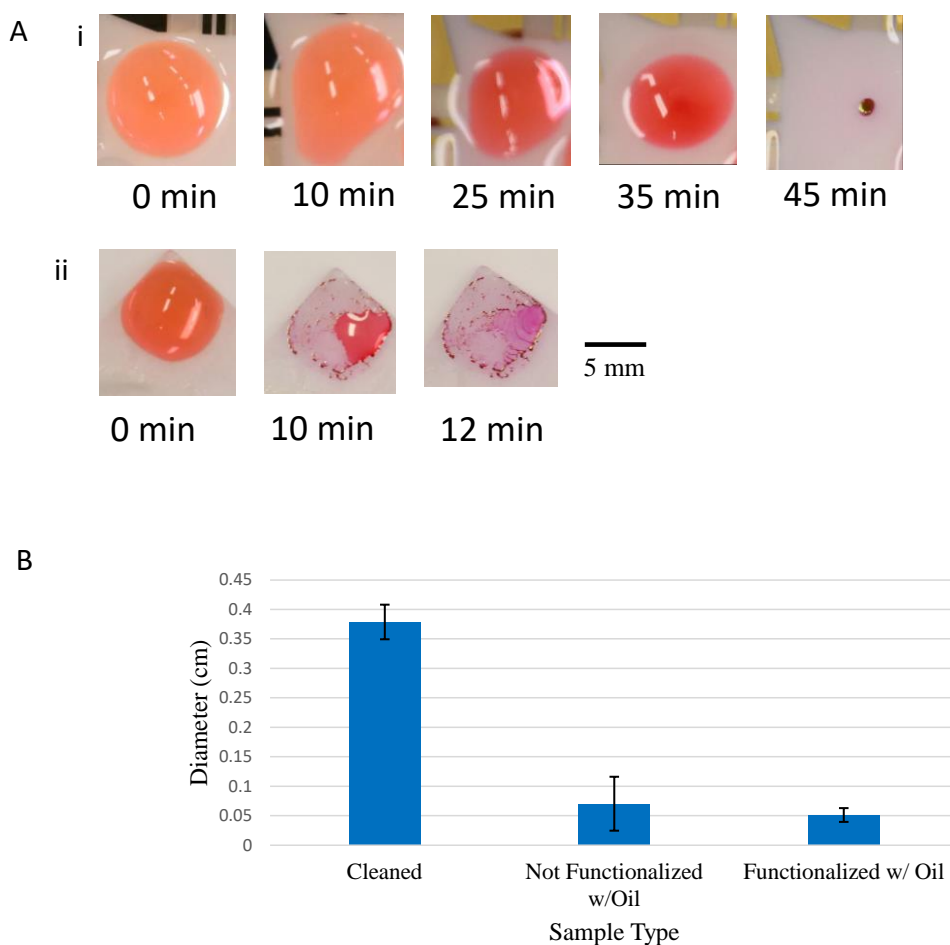
Figure 39. The evaporation of droplets containing rhodimine dye on a heated LiNbO₃ surface. A) Snapshots of droplets at different times throughout the evaporation for a (i) Krytox 103 liquid layer and (ii) non-functionalized surface. B) A plot of the final droplet diameter for a cleaned surface, a cleaned surface with Krytox 103 oil and a functionalized surface with Krytox 103 oil.

4.4 Discussion

4.4.1 Surface Functionalization Effectiveness

From the contact angle before and after the functionalization protocol (Figure 32) it is clear that the hydrophobicity of the LiNbO₃ has increased. A good cutoff value for evaluating hydrophobicity with contact angle is 90°. The cleaned surface has a contact angle of 22±4.4°, well below 90° showing high hydrophilicity. The functionalized surface showed high

54

hydrophobicity with a contact angle above 90° of 105.6±3.8 °. This is consistent with the

literature value of contact angle for silane functionalized $LiNbO_3$ (110°)[91].

The monolayer of silane had been attached to the surface, but it had not been tested

whether the oil layer would be trapped. The microscope images shown in Figure 31 show a

blotchiness that is indicative of a non-uniform monolayer of silane. A non-uniform layer could

explain the dewetting of the surface seen in Figure 34. The tilt angle experiment was conducted

to determine if this apparent uneven layer of silane held the oil on the surface well enough to

allow the droplet to slide easily. With sliding angles around 1-2 degrees when functionalized it is

clear that the surface functionalization was trapping the liquid layer and allowing for easy

hydroplaning. Without it the droplet pushes the oil out from under it and makes contact with the

hydrophilic surface. It then sticks to the surface and does not move when tilted. The blotchiness

may indicate an uneven monolayer but it appears to be trapping the oil on the surface at least

temporarily. However, as others have been able to move droplets with just silanization and no oil

it is clear this process can be improved[47,91]. Perhaps more rigorous cleaning in a cleanroom

setting or using fresher silane could help. Also, due to the dewetting, the oil has to be re-spread

on the surface before every use. This will lead to oil loss and layer oil thinning over time.

It was also determined that the oil could not be removed from the surface without altering

the surface properties. Figure 36 showed that after cleaning with NOVAC solution and

reapplication of the oil the signal changed significantly. This could be due to the NOVAC

removing the surface functionalization or the NOVAC itself being trapped on the surface by the

monolayer. The NOVAC is also a fluorinated liquid and could get trapped to some extent, so that

the surface is never truly reverted back to a non-liquid-infused state.

4.4.2 Moving a Droplet

With a functioning slippery surface layer the amount of energy required to push a droplet on the surface is significantly lowered[88,94,96]. Without it the droplet would not move or would violently fly off the surface[13,72,73], spread (Figure 37B), or evaporate rapidly depending on the magnitude of the energy input. However, when the functionalized 100 MHz SAW device was connected to the synthesizer and signal processing system and a droplet was placed on the surface, it did not move at all. Ripples were observed propagating through the oil from the IDT, but the droplet did not move from its position. There could be a few reasons for this. First of all, the attenuation due to the oil is reducing the intensity of the wave so much that very little of the energy is making it to the droplet. In order to minimize attenuation, the oil layer was made as thin as possible (around 15 μm) and designed a lower frequency device (60 MHz). Another possible reason for the lack of droplet movement could be the imperfect surface functionalization. While the sliding angle was shown to be acceptable it is possible that it was damaged during the loading process into the circuit board or something went wrong with the functionalization of this particular device.

We saw better results from the 60 MHz device. Although the attenuation was also severe the droplet could be moved. Figure 36 showed that the $|S_{21}|$ transmission coefficient amplitude dropped to noise levels just as the 100 MHz device had, indicating that power was not making it the other side of the device. However, that simply means that all the energy is being dissipated to the oil. The lower frequency allows for a slower dissipation and greater penetration of the energy into the oil. This allows for the energy to not only reach the droplet but also push it a distance before completely attenuating. The distance between the IDTs was 1 cm and with such a viscous oil it is expected that the signal does not reach the other IDT. Figure 37 demonstrates that unlike

the 100 MHz devices, the energy was now making it to the droplet at a high enough intensity to move it along the surface. A cleaned device will see the droplet elongate and spread out over the surface due to the hydrophilic substrate. The imperfect silane monolayer does not allow for easy translation so the droplet elongates, which is consistent with what is reported in the literature[88,97]. At higher powers it is possible to get the droplet to slide but erratically. With an evenly spread oil layer the droplet slides easily across the surface and maintains its shape. However, due to the dewetting over time the oil layer will have to be reset every so often, leading to gradual thinning unless more oil is added. A dewetted surface saw slight deformation of the droplet but no translation or elongation. This is likely due to the residual oil attenuating and scattering the power before it hits the droplet.

It was also of interest to determine the best conditions for moving a droplet. Figure 38 gives a good picture of how the droplet size and oil layer thickness played a role in the speed and effectiveness of the SAW in moving the droplet. The speed was generally found to be highest for the smaller droplets and the thinnest oil layer. The maximum speed measured was 0.45±0.11 mm/s with a 5 μL droplet on an 8.3 μm oil layer. This is most likely due to the fact that a thin oil layer minimizes the attenuation of the wave and a smaller droplet is easier to push around. The large variation can be attributed to the droplets sometimes being pushed off to the side during the measurements, reducing the measured velocity. SAW will naturally push droplets to the side over time so some sort of track system will have to be put in place to prevent this. Other SAW devices or tracks of patterned functionalization could be used to do this[9]. The surfaces would also dewet after extended use leading to occasional sticking. Also, especially for the thicker oil layers, the droplets would start to move backwards at times. This could be due to oil displaced behind them, creating a divot and causing the droplet to slide downhill back towards the IDT, as

described by Zhang et al. 2018[86]. Sticking could be caused by large spots of imperfect functionalization causing dewetting and allowing for hydrophilic dust and debris to attach to the surface, which the droplet could get hooked on[97]. Repeated insertion and removal of the device from the setup could potentially damage the surface functionalization if one is not careful. The functionalization protocol needs to be improved to provide a more stable silane monolayer. Perhaps the use of fresher silane or a longer plasma oven bake step would help. Also the oil layer should be reapplied often to prevent contaminants in the air from landing on the surface.

4.4.3 Droplet Concentration Effectiveness

Moving a droplet around a surface is useful but it is often what the droplets contain that is of interest. Small concentrations of particles can be manipulated on a surface via a droplet of its solvent and then concentrated to provide better sensitivity during analysis[4,7]. Droplets can be concentrated on a surface through evaporation but only if the coffee ring effect is prevented by the liquid layer[32,45,88,98]. The liquid layer does this by ensuring that the droplet and particles within do not actually come in contact with the surface. The edges of the droplet do not become pinned to the surface and the particles do not concentrate there[88,92,98]. This also prevents contamination of the surface. It was shown in Figure 38 that without the oil on the surface the coffee ring effect was prevalent as previously reported in Yang et al. 2016[98]. The diameter of the dried stain measured approximately 3.7 mm while the diameter with oil measured between 0.5 and 1 mm. The functionalization also played a role in the consistency of the concentration. There was a slight increase in variability without the silane monolayer. This was again most likely due to dewetting on the surface. Any dewetting would allow contact between the surface and the droplet allowing for the coffee ring effect to occur. Another effect of the liquid layer previously mentioned is that it slows the rate of evaporation[93]. As discussed earlier in the chapter a

wrapping layer forms around a droplet on a liquid layer[93,94]. This impedes the water molecules making it more difficult for them to escape. Without oil the droplet took less than 15 minutes to full evaporate, but over 40 minutes with oil. The oil allows for a more gradual and controlled evaporation of droplets. This can be combined with the movement of droplets on the surface to create a multifunctional system. Droplets can be moved along the surface, mixed, and split. Then once that is done they could be stopped and concentrated for analysis.

4.5 Conclusions

The use of surface functionalization to perform channel-less microfluidics has been explored. The surface was successfully functionalized with a layer of silane, although it seems to be imperfect due to some visual blotchiness and significant dewetting. Despite this, the sliding angle was an average of $2.33\pm1.33°$ without draining and $4.52\pm0.915°$ after draining to a thickness of 8.34 μm, indicating a functional oil layer even with low amounts of oil. When power was applied to the 100 MHz SAW and a droplet was on the surface there was no movement but it could be concentrated. There was indication that the SAW was working but the power was not enough to move the droplet. The 60 MHz device fixed this issue allowing for both movement and concentration with the functionalized $LiNbO_3$ surface. Functionalization tracks will be implemented in the future to keep the droplet moving straight and not off to the side. The next step will be to combine these functionalities to create a multifunctional droplet analysis system. Using this technique with blood samples could enable improved manipulation, detection, and analysis of small, low concentration pancreatic cancer biomarkers without the need for microfluidic channels.

CHAPTER 5:

CONCLUSION AND OUTLOOK

5.1 Overview

The work completed in this project has laid the groundwork for exploring the possibilities of using SAW for diagnostic applications. This is especially useful for diseases such as pancreatic cancer which need to be diagnosed early by identifying small, low concentration biomarkers in the blood. An easy-to-use consistent circuit board interface for the SAW devices was designed. The use of pogo pins allowed for plug-and-play capabilities speeding up the ability to do various different tests with different devices. Two different SAW devices were then tested with this interface. A 100 MHz device previously designed for cell lysis was initially tested. However, due to the high frequency the acoustic wave was severely attenuated by the materials used in the work. A new SAW device operating at the optimal frequency of 60 MHz was tested and found to exhibit less attenuation and increase power delivery to the microfluidic system.

These SAW devices were either bonded to PDMS microfluidic channels or were functionalized with silane and coated with fluorinated oil. There were difficulties in attaching the PDMS to the surface of the $LiNbO_3$ but increasing the oxygen concentration during plasma treatment and covering prominently leaking areas with silicone provided a solution. Polystyrene microparticles could be viewed in the channel under a microscope and movement due to the SAW was observed. However, as the SAW agitated the particles they stuck to the ceiling of the channel and no separation was observed. By using the lower frequency devices and adding surfactant to the channel we hope to prevent this from happening. The functionalization of the surface allows for droplet and particle manipulation without having to worry about a PDMS

channel. When tested with the 100 MHz devices there was visible disturbance of the oil but no movement of the droplet. It was found that the use of 60 MHz devices and a thinner oil layer allowed for effective droplet movement on the surface. Thicker oil layers tended to lead to slower droplet movement and even backwards movement not explained in this work. The oil layer also allowed for effective droplet concentration and prevention of the coffee ring effect when heated by a Peltier device.

5.2 Future Directions

With the groundwork set for this project the next steps will involve integrating our setup into a diagnostic device. The microfluidic channel will be tested with microparticles varying in size from 7 μm to 20 μm in diameter. If the device developed in this work is able to manipulate and separate them, then we can test with even smaller particles on the scale of exosomes (100 nm diameter)[12]. With a working separation device we will work with the Zhang lab at Dartmouth to determine how to best integrate it with their system.

The next step for the surface functionalization is to combine the droplet translation with the evaporation and create a system to manipulate droplets and concentrate them on command for further analysis. Integrating this with arrays of IDTs could allow us to perform multiple functionalities, including droplet splitting, merging, mixing, and ejection on the same chip. Easy and controlled manipulation of small micro or nanodroplets can open up a many possibilities with regards to diagnostics. Pancreatic cancer diagnostics using open microfluidics and SAW can improve upon the sensitivity of liquid biopsy diagnostics by isolating particles of interest, facilitating chemical reactions, and then concentrating them on demand. This multifunctionality makes the technology studied extremely versatile. The SAW devices can also pattern particles into arrays that can run multiple diagnostic tests at once on multiple samples.

REFERENCES

1. American Cancer Society. Facts and FIgures 2021. https://www.cancer.org/cancer/pancreatic-cancer/about/key-statistics.html#references. Published 2021.

2. Hidalgo M. Pancreatic Cancer. *N Engl J Med*. 2010;362(17):1605-1617. doi:10.1056/NEJMra0901557

3. Neoptolemos JP, Urrutia R, Abbruzzese JL, Büchler MW. Pancreatic Cancer. *Pancreat Cancer*. 2018;388(10039):1-1661. doi:10.1007/978-1-4939-7193-0

4. Poruk KE, Firpo MA, Adler DG, Mulvihill SJ. Screening for pancreatic cancer: Why, how, and who? *Ann Surg*. 2013;257(1):17-26. doi:10.1097/SLA.0b013e31825ffbfb

5. Yeo LY, Friend JR. Surface Acoustic Wave Microfluidics. *Annu Rev Fluid Mech*. 2014;46(1):379-406. doi:10.1146/annurev-fluid-010313-141418

6. Ding X, Li P, Lin SCS, et al. Surface acoustic wave microfluidics. *Lab Chip*. 2013;13(18):3626-3649. doi:10.1039/c3lc50361e

7. Wu M, Ozcelik A, Rufo J, Wang Z, Fang R, Jun Huang T. Acoustofluidic separation of cells and particles. *Microsystems Nanoeng*. 2019;5(1). doi:10.1038/s41378-019-0064-3

8. Sajeesh P, Sen AK. Particle separation and sorting in microfluidic devices: A review. *Microfluid Nanofluidics*. 2014;17(1):1-52. doi:10.1007/s10404-013-1291-9

9. Wixforth A. Acoustically Driven Programmable Microfluidics for Biological and Chemical Applications. *J Lab Autom*. 2006;11(6):399-405. doi:10.1016/j.jala.2006.08.001

10. Xi H-D, Zheng H, Guo W, et al. Active droplet sorting in microfluidics: a review. *Lab Chip*. 2017. doi:10.1039/c6lc01435f

11. Rocha-Gaso MI, March-Iborra C, Montoya-Baides Á, Arnau-Vives A. Surface generated acoustic wave biosensors for the detection of pathogens: A review. *Sensors*. 2009;9(7):5740-5769. doi:10.3390/s9095740

12. Go DB, Atashbar MZ, Ramshani Z, Chang HC. Surface acoustic wave devices for chemical sensing and microfluidics: A review and perspective. *Anal Methods*. 2017;9(28):4112-4134. doi:10.1039/c7ay00690j

13. Lyford TJ, Millard PJ, Da Cunha MP. Cell lysisa using surface acoustic wave devices for sensor applications. *IEEE Int Ultrason Symp IUS*. 2012:1216-1219. doi:10.1109/ULTSYM.2012.0303

14. Morgans D. Surface acoustic wave devices and applications. 2. Pulse compression systems. *Ultrasonics*. 1973;11(5):211-217. doi:10.1016/0041-624X(73)90232-1

15. Campbell CK. Applications of Surface Acoustic and Shallow Bulk Acoustic Wave Devices. *Proc IEEE*. 1989;77(10):1453-1484. doi:10.1109/5.40664

16. Weigel R, Morgan DP, Owens JM, et al. Microwave acoustic materials, devices, and applications. *IEEE Trans Microw Theory Tech*. 2002;50(3):738-749. doi:10.1109/22.989958

17. Gulyaev Y V. Review of shear surface acoustic waves in solids. *IEEE Trans Ultrason Ferroelectr Freq Control*. 1998;45(4):935-938. doi:10.1109/58.710563

18. Tyagi S, Mahesh VG. Saw and Interdigital Transducers. *Int J Sci Eng Res*. 2012;3(12):1-4. http://www.ijser.org.

19. Hays RM, Hartmann CS. Surface-Acoustic-Wave Devices for Communications. *Proc IEEE*. 1976;64(5):652-671. doi:10.1109/PROC.1976.10190

20. Shi J, Huang H, Stratton Z, Huang Y, Huang TJ. Continuous particle separation in a microfluidic channel via standing surface acoustic waves (SSAW). *Lab Chip*. 2009;9(23):3354. doi:10.1039/b915113c

21. Huang X, Li Z, Yu Z, Deng X, Xin Y, Jesionowski T. Recent Advances in the Synthesis, Properties, and Biological Applications of Platinum Nanoclusters. *J Nanomater*. 2019;2019. doi:10.1155/2019/6248725

22. Calabrese GS, Wohltjen H, Roy MK. Surface Acoustic Wave Devices as Chemical Sensors in Liquids. Evidence Disputing the Importance of Rayleigh Wave Propagation. *Anal Chem*. 1987;59(6):833-837. doi:10.1021/ac00133a010

23. Gronewold TMA. Surface acoustic wave sensors in the bioanalytical field: Recent trends and challenges. *Anal Chim Acta*. 2007;603(2):119-128. doi:10.1016/j.aca.2007.09.056

24. Wohltjen H, Dessy R. Surface Acoustic Wave Probe for Chemical Analysis. I. Introduction and Instrument Description. *Anal Chem*. 1979;51(9):1458-1464. doi:10.1021/ac50045a024

25. Berkenpas E, Millard P, Pereira da Cunha M. Detection of Escherichia coli O157:H7 with langasite pure shear horizontal surface acoustic wave sensors. *Biosens Bioelectron*. 2006;21(12):2255-2262. doi:10.1016/j.bios.2005.11.005

26. Liu X, Wang JY, Mao XB, Ning Y, Zhang GJ. Single-Shot Analytical Assay Based on Graphene-Oxide-Modified Surface Acoustic Wave Biosensor for Detection of Single-Nucleotide Polymorphisms. *Anal Chem*. 2015;87(18):9352-9359. doi:10.1021/acs.analchem.5b02121

27.	Friend JR, Yeo LY, Arifin DR, Mechler A. Evaporative self-assembly assisted synthesis of polymeric nanoparticles by surface acoustic wave atomization. *Nanotechnology*. 2008;19(14). doi:10.1088/0957-4484/19/14/145301

28.	Qi A, Friend JR, Yeo LY, Morton DAV, McIntosh MP, Spiccia L. Miniature inhalation therapy platform using surface acoustic wave microfluidic atomization. *Lab Chip*. 2009;9(15):2184-2193. doi:10.1039/b903575c

29.	Luong T-D, Nguyen N-T. Surface acoustic wave driven microfluidics - A review. *Micro Nanosyst*. 2010;2(3):1-9.

30.	Park J, Destgeer G, Kim H, Cho Y, Sung HJ. In-droplet microparticle washing and enrichment using surface acoustic wave-driven acoustic radiation force. *Lab Chip*. 2018;18(19):2936-2945. doi:10.1039/c8lc00733k

31.	Fornell A, Barbe L, Hjort K. On-chip background dilution in droplets with high particle recovery using acoustophoresis On-chip background dilution in droplets with high particle recovery using acoustophoresis. 2019;064123(December). doi:10.1063/1.5129256

32.	Luo JT, Geraldi NR, Guan JH, McHale G, Wells GG, Fu YQ. Slippery Liquid-Infused Porous Surfaces and Droplet Transportation by Surface Acoustic Waves. *Phys Rev Appl*. 2017;7(1):1-9. doi:10.1103/PhysRevApplied.7.014017

33.	Collignon S, Friend J, Yeo L. Planar microfluidic drop splitting and merging. *Lab Chip*. 2015;15(8):1942-1951. doi:10.1039/c4lc01453g

34.	Destgeer G, Lee KH, Jung JH, Alazzam A, Sung HJ. Continuous separation of particles in a PDMS microfluidic channel via travelling surface acoustic waves (TSAW). *Lab Chip*. 2013;13(21):4210-4216. doi:10.1039/c3lc50451d

35.	Lee K, Shao H, Weissleder R, Lee H, Hospital MG. Acoustic purification of Extracellular Microvesicles. 2015;9(3):2321-2327. doi:10.1021/nn506538f.Acoustic

36.	Chen-Glasser M, Li P, Ryu J, Hong S. Piezoelectric Materials for Medical Applications. In: Vassiliadis S, Matsouka D, eds. *Piezoelectricity: Organic and Inorganic Materials and Applications*. IntechOpen; 2018.

37.	Campbell C. *Surface Acoustic Wave Devices for Mobil and Wrieless Communications*.; 1998.

38.	Morgan DP. *Surface-Wave Devices for Signal Processing*. Elsevier Ltd; 1985.

39.	Currie PK, Hayes MA. VISCOELASTIC RAYLEIGH WAVES. *Q Appl Mathmatics*. 1977;35(1):35-53.

40. Wang Z, Zhe J. Recent advances in particle and droplet manipulation for lab-on-a-chip devices based on surface acoustic waves. *Lab Chip*. 2011;11(7):1280-1285. doi:10.1039/c0lc00527d

41. Versiani AF, Andrade LM, Martins EMN, et al. Gold nanoparticles and their applications in biomedicine. *Future Virol*. 2016;11(4):293-309. doi:10.2217/fvl-2015-0010

42. Nam J, Lim H, Shin S. Manipulation of microparticles using surface acoustic wave in microfluidic systems: A brief review. *Korea Aust Rheol J*. 2011;23(4):255-267. doi:10.1007/s13367-011-0031-5

43. Wang K, Zhou W, Lin Z, et al. Sorting of tumour cells in a microfluidic device by multi-stage surface acoustic waves. *Sensors Actuators, B Chem*. 2018. doi:10.1016/j.snb.2017.12.013

44. Shi J, Ahmed D, Mao X, Lin S-CS, Lawit A, Huang TJ. Acoustic tweezers: patterning cells and microparticles using standing surface acoustic waves (SSAW). *Lab Chip*. 2009;9(20):2890. doi:10.1039/b910595f

45. Connacher W, Zhang N, Huang A, et al. Micro/nano acoustofluidics: Materials, phenomena, design, devices, and applications. *Lab Chip*. 2018;18(14):1952-1996. doi:10.1039/c8lc00112j

46. Nama N, Barnkob R, Mao Z, Kähler CJ, Costanzo F, Huang TJ. Numerical study of acoustophoretic motion of particles in a PDMS microchannel driven by surface acoustic waves. *Lab Chip*. 2015;15(12):2700-2709. doi:10.1039/c5lc00231a

47. Wixforth A, Strobl C, Gauer C, Toegl A, Scriba J, Guttenberg Z V. Acoustic manipulation of small droplets. *Anal Bioanal Chem*. 2004;379(7-8):982-991. doi:10.1007/s00216-004-2693-z

48. Vanneste J, Bühler O. Streaming by leaky surface acoustic waves. *Proc R Soc A Math Phys Eng Sci*. 2011;467(2130):1779-1800. doi:10.1098/rspa.2010.0457

49. Louis K. On the acoustic radiation pressure on spheres. *Proc R Soc London Ser A - Math Phys Sci*. 1934;147(861):212-240. doi:10.1098/rspa.1934.0215

50. Knuuttila J V., Vartiainen JJ, Koskela J, Plessky VP, Hartmann CS, Salomaa MM. Bulk-acoustic waves radiated from low-loss surface-acoustic-wave resonators. *Appl Phys Lett*. 2004;84(9):1579-1581. doi:10.1063/1.1650557

51. Hartmann CS, Plessky VP. Experimental measurements of propagation, attenuation, reflection and scattering of leaky waves in Al electrode gratings on 41°, 52° and 64°-LiNbO3. *Proc IEEE Ultrason Symp*. 1993;2:1247-1250. doi:10.1109/ultsym.1993.339607

52.   Hartono D, Liu Y, Tan PL, Then XYS, Yung LYL, Lim KM. On-chip measurements of cell compressibility via acoustic radiation. *Lab Chip*. 2011;11(23):4072-4080. doi:10.1039/c1lc20687g

53.   Nilsson A, Petersson F, Jönsson H, Laurell T. Acoustic control of suspended particles in micro fluidic chips. *Lab Chip*. 2004;4(2):131-135. doi:10.1039/b313493h

54.   Guldiken R, Jo MC, Gallant ND, Demirci U, Zhe J. Sheathless size-based acoustic particle separation. *Sensors*. 2012;12(1):905-922. doi:10.3390/s120100905

55.   Yosioka K, Kawasima Y. Acoustic radiation pressure on a compressible sphere. *Acustica*. 1955;5.

56.   Berkenpas E, Bitla S, Millard P, Da Cunha MP. Pure shear horizontal SAW biosensor on langasite. *IEEE Trans Ultrason Ferroelectr Freq Control*. 2004. doi:10.1109/TUFFC.2004.1367479

57.   Berkenpas E, Millard P, Da Cunha MP. Novel O157:H7 E. coll detector utilizing a langasite surface acoustic wave sensor. In: *Proceedings of IEEE Sensors*. ; 2005. doi:10.1109/ICSENS.2005.1597930

58.   Zhang Z, Emanetoglu NW, Saraf G, et al. DNA immobilization and SAW response in ZnO nanotips grown on LiNbO 3 substrates. *IEEE Trans Ultrason Ferroelectr Freq Control*. 2006;53(4):786-791. doi:10.1016/j.jasms.2006.02.016

59.   Taylor JJ, Jaedicke KM, van de Merwe RC, et al. A Prototype Antibody-based Biosensor for Measurement of Salivary MMP-8 in Periodontitis using Surface Acoustic Wave Technology. *Sci Rep*. 2019;9(1):1-9. doi:10.1038/s41598-019-47513-w

60.   Bröker P, Lücke K, Perpeet M, Gronewold TMA. A nanostructured SAW chip-based biosensor detecting cancer cells. *Sensors Actuators, B Chem*. 2012;165(1):1-6. doi:10.1016/j.snb.2011.11.022

61.   Ding X, Peng Z, Lin SCS, et al. Cell separation using tilted-angle standing surface acoustic waves. *Proc Natl Acad Sci U S A*. 2014;111(36):12992-12997. doi:10.1073/pnas.1413325111

62.   Yeo LY, Friend JR. Ultrafast microfluidics using surface acoustic waves. In: *Biomicrofluidics*. ; 2009. doi:10.1063/1.3056040

63.   Lee K, Shao H, Weissleder R, Lee H. Acoustic purification of extracellular microvesicles. *ACS Nano*. 2015. doi:10.1021/nn506538f

64.   Ding X, Lin S-CS, Kiraly B, et al. On-chip manipulation of single microparticles, cells, and organisms using surface acoustic waves. doi:10.1073/pnas.1209288109/-/DCSupplemental

65. Wong TS, Kang SH, Tang SKY, et al. Bioinspired self-repairing slippery surfaces with pressure-stable omniphobicity. *Nature*. 2011;477(7365):443-447. doi:10.1038/nature10447

66. Luong TD, Phan VN, Nguyen NT. High-throughput micromixers based on acoustic streaming induced by surface acoustic wave. *Microfluid Nanofluidics*. 2011;10(3):619-625. doi:10.1007/s10404-010-0694-0

67. Shiokawa S, Matsui Y, Ueda T. Study on saw streaming and its application to fluid devices. *Jpn J Appl Phys*. 1990;29:137-139. doi:10.7567/JJAPS.29S1.137

68. Bennès J, Alzuaga S, Ballandras S, Chérioux F, Bastien F, Manceau JF. Droplet ejector using surface acoustic waves. *Proc - IEEE Ultrason Symp*. 2005;2(c):823-826. doi:10.1109/ULTSYM.2005.1602976

69. Duerig TW. *Present and Future Applications of Shape Memory and Superelastic Materials*. Vol 360.; 1995. doi:10.1557/proc-360-497

70. Castro J, Ramesan S, Rezk A, Yeo L. Continuous Tuneable Droplet Ejection via Pulsed. *Soft Matter*. 2018.

71. Rajapaksa A, Qi A, Yeo LY, Coppel R, Friend JR. Enabling practical surface acoustic wave nebulizer drug delivery via amplitude modulation. *Lab Chip*. 2014;14(11):1858-1865. doi:10.1039/c4lc00232f

72. Alvarez M, Friend J, Yeo LY. Rapid generation of protein aerosols and nanoparticles via surface acoustic wave atomization. *Nanotechnology*. 2008;19(45). doi:10.1088/0957-4484/19/45/455103

73. Lyford T. Development of a Surface Acoustic Wave Device for the Lysis of Bacterial and Red Blood Cells. 2017.

74. Ramo S, Whinnery JR, Van Duzer T. *Fields and Waves in Communication Electronics*. 3rd ed. John Wiley & Sons, Ltd; 1994.

75. Pozer D. *Microwave Engineering*. 3rd ed. (Zobrist B, Kulck P, Kincheloe K, Aiello G, Grobe CC, eds.). John Wiley & Sons, Ltd; 2011.

76. Dellsperger F. Circuit Design with Smith Chart. 2018. http://www.fritz.dellsperger.net/smith.html.

77. University IS. Acoustic Attenuation. https://www.nde-ed.org/Physics/Waves/attenuation.xhtml. Accessed April 4, 2021.

78. Winkler A, Brünig R, Faust C, Weser R, Schmidt H. Towards efficient surface acoustic wave (SAW)-based microfluidic actuators. *Sensors Actuators, A Phys*. 2016;247:259-268. doi:10.1016/j.sna.2016.06.006

79. Inc. BPO. TABLE OF ULTRASONIC PROPERTIES. https://www.bostonpiezooptics.com/ultrasonic-properties.

80. Jo MC, Guldiken R. Effects of polydimethylsiloxane (PDMS) microchannels on surface acoustic wave-based microfluidic devices. *Microelectron Eng*. 2014;113:98-104. doi:10.1016/j.mee.2013.07.021

81. Wu H, Huang B, Zare RN. Construction of microfluidic chips using polydimethylsiloxane for adhesive bonding. *Lab Chip*. 2005;5(12):1393-1398. doi:10.1039/b510494g

82. Sunkara V, Park DK, Cho YK. Versatile method for bonding hard and soft materials. *RSC Adv*. 2012;2(24):9066-9070. doi:10.1039/c2ra20880f

83. Gijs MAM. Magnetic bead handling on-chip: New opportunities for analytical applications. *Microfluid Nanofluidics*. 2004;1(1):22-40. doi:10.1007/s10404-004-0010-y

84. Cho CF, Lee K, Speranza MC, et al. Design of a Microfluidic Chip for Magnetic-Activated Sorting of One-Bead-One-Compound Libraries. *ACS Comb Sci*. 2016;18(6):271-278. doi:10.1021/acscombsci.5b00180

85. Yeo LY, Friend JR, Li H. Nanoparticle patterning in a microfluidic drop induced by surface acoustic waves. *Proc - IEEE Ultrason Symp*. 2009:606-608. doi:10.1109/ULTSYM.2009.5441910

86. Zhang SP, Lata J, Chen C, et al. Digital acoustofluidics enables contactless and programmable liquid handling. *Nat Commun*. 2018;9(1):1-11. doi:10.1038/s41467-018-05297-z

87. Guttenberg Z, Müller H, Habermüller H, et al. Planar chip device for PCR and hybridization with surface acoustic wave pump. *Lab Chip*. 2005;5(3):308-317. doi:10.1039/b412712a

88. Regan DP, Howell C. Droplet manipulation with bioinspired liquid-infused surfaces: A review of recent progress and potential for integrated detection. *Curr Opin Colloid Interface Sci*. 2019;39:137-147. doi:10.1016/j.cocis.2019.01.012

89. Che P, Heng L, Jiang L. Lubricant-Infused Anisotropic Porous Surface Design of Reduced Graphene Oxide Toward Electrically Driven Smart Control of Conductive Droplets' Motion. *Adv Funct Mater*. 2017;27(22):1-9. doi:10.1002/adfm.201606199

90. Khalil KS, Mahmoudi SR, Abu-Dheir N, Varanasi KK. Active surfaces: Ferrofluid-impregnated surfaces for active manipulation of droplets. *Appl Phys Lett*. 2014;105(4). doi:10.1063/1.4891439

91. Ai Y, Marrone BL. Droplet translocation by focused surface acoustic waves. *Microfluid Nanofluidics*. 2012;13(5):715-722. doi:10.1007/s10404-012-0990-y

92. Howell C, Grinthal A, Sunny S, Aizenberg M, Aizenberg J. Designing Liquid-Infused Surfaces for Medical Applications: A Review. *Adv Mater*. 2018;30(50). doi:10.1002/adma.201802724

93. Guan JH, G.Wells G, McHale G, Xu B. Evaporation of Sessile Droplets on Slippery Liquid-Infused Porous Surfaces (SLIPS). *Crit Stud Secur*. 2014;2(2):210-222.

94. Kreder MJ, Daniel D, Tetreault A, et al. Film Dynamics and Lubricant Depletion by Droplets Moving on Lubricated Surfaces. *Phys Rev X*. 2018;8(3):31053. doi:10.1103/PhysRevX.8.031053

95. Bennès J, Ballandras S, Chérioux F. Easy and versatile functionalization of lithium niobate wafers by hydrophobic trichlorosilanes. *Appl Surf Sci*. 2008;255(5 PART 1):1796-1800. doi:10.1016/j.apsusc.2008.06.031

96. Keiser A, Keiser L, Clanet C, Quéré D. Drop friction on liquid-infused materials. *Soft Matter*. 2017;13(39):6981-6987. doi:10.1039/c7sm01226h

97. Daniel D, Timonen JVI, Li R, Velling SJ, Aizenberg J. Oleoplaning droplets on lubricated surfaces. *Nat Phys*. 2017;13(10):1020-1025. doi:10.1038/nphys4177

98. Yang S, Dai X, Stogin BB, Wong TS. Ultrasensitive surface-enhanced Raman scattering detection in common fluids. *Proc Natl Acad Sci U S A*. 2016;113(2):268-273. doi:10.1073/pnas.1518980113
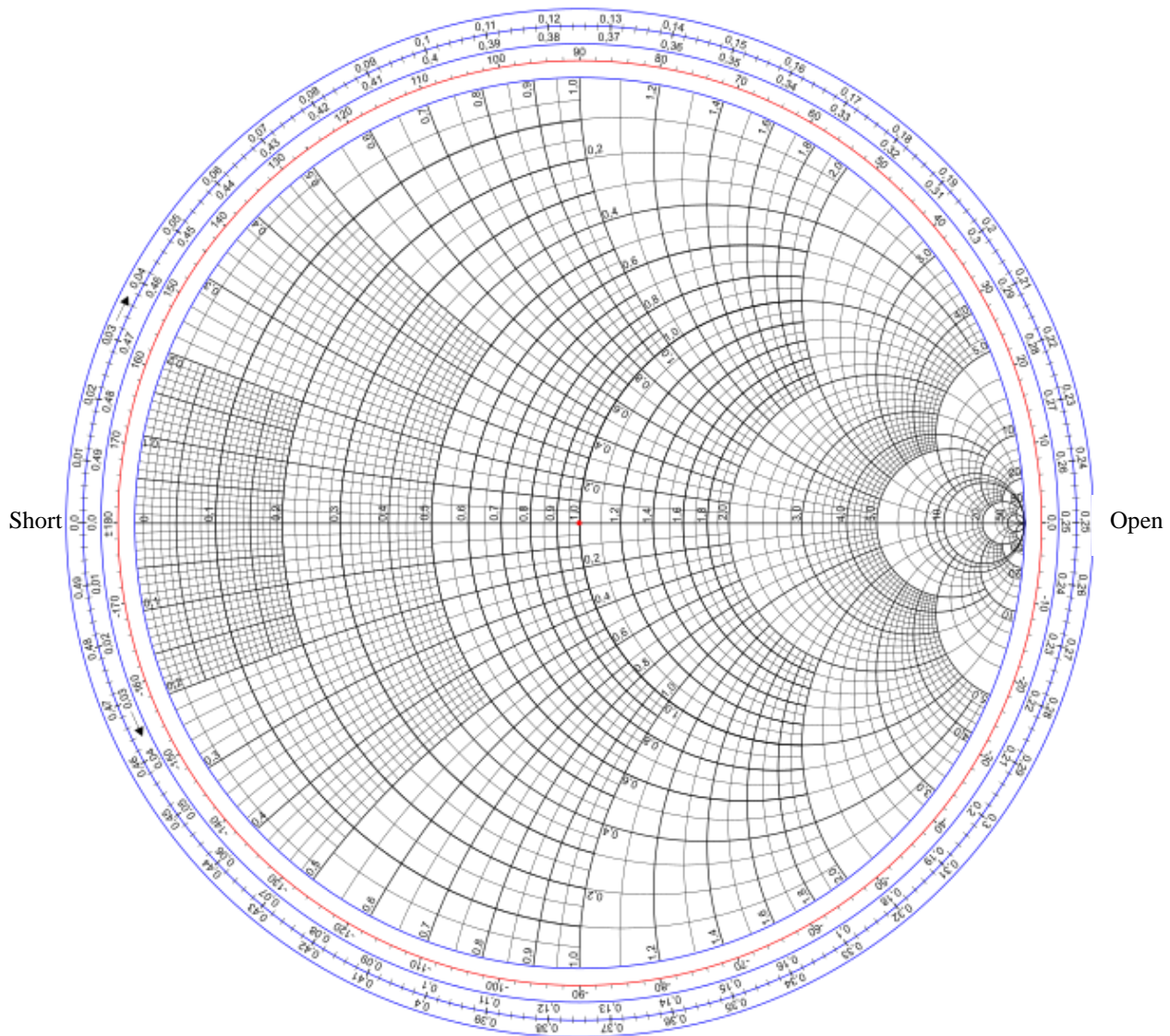
Figure 1A. Example of a Smith Chart. The center of the chart represents a reflection coefficient of zero, and thus is matched to the reference impedance of the system, usually 50 Ω. The right hand side of the chart indicates an open circuit impedance load and the left indicates a short circuit impedance load. More information on reading the Smith chart can be found in Fields and Waves in Communication Electronics 3rd Edition[74].

BIOGRAPHY OF THE AUTHOR

Joel Tewksbury was born in Presque Isle, Maine in October of 1996. He attended and graduated from Presque Isle High School in 2014. He went on to receive a Bachelor of Science in Engineering from Duke University in 2018. During his undergraduate career he worked in the lab of Dr. Ashutosh Chilkoti and under the guidance of Parisa Yousefpour performing research on biospecific protein conjugates for targeted drug delivery of doxorubicin to cancer cells. He was a co-author on the paper "Conjugate of Doxorubicin to Albumin-Binding Peptide Outperofrms Aldoxoruicin" in *Small*. He moved back to Maine in 2019 to pursue a Masters of Science in Biomedical Engineering before applying to medical school. Joel is a candidate for the Masters of Science in Biomedical Engineering from the University of Maine in May 2021.